Biomechan Model Mechanobiol (2005) 3: 147–171
DOI 10.1007/s10237-004-0047-6

ORIGINAL PAPER

A. Menzel

Modelling of anisotropic growth in biological tissues

A new approach and computational aspects

Received: 10 December 2003 / Accepted: 3 May 2004 / Published online: 15 October 2004
© Springer-Verlag 2004

Abstract In this contribution, we develop a theoretical and computational framework for anisotropic growth phenomena. As a key idea of the proposed phenomenological approach, a fibre or rather structural tensor is introduced, which allows the description of transversely isotropic material behaviour. Based on this additional argument, anisotropic growth is modelled via appropriate evolution equations for the fibre while volumetric remodelling is realised by an evolution of the referential density. Both the strength of the fibre as well as the density follow Wolff-type laws. We however elaborate on two different approaches for the evolution of the fibre direction, namely an alignment with respect to strain or with respect to stress. One of the main benefits of the developed framework is therefore the opportunity to address the evolutions of the fibre strength and the fibre direction separately. It is then straightforward to set up appropriate integration algorithms such that the developed framework fits nicely into common, finite element schemes. Finally, several numerical examples underline the applicability of the proposed formulation.

1 Introduction

The development of appropriate models for biological tissues that capture at least some of the essential biochemical and biophysical or rather biomechanical effects is a fundamental task. Both hard tissues, such as bones and teeth, or soft tissues, such as ligaments, tendons, muscles, skin and vessels, have attracted study. Several outstanding monographs document the rapid development of this important scientific field of activity; for example Schneck (1990), Fung (1993), Humphrey (2002) and Murray (2002), the review articles by Taber (1995) and Cowin (1999b) or the contributions in Cowin (2001), Cowin and Humphrey (2000), as well as Holzapfel and Ogden (2003). A typical classification of the biomechanical behaviour of tissues is thereby introduced by distinguishing between passive response, active response and remodelling. One particular property of the first and second category consists in the assumption of conservation of mass, while the latter category assembles effects like growth phenomena and the evolution of internal structures.

The modelling of the passive response of, say, soft tissues as arteries is highly developed these days; see Holzapfel (2001) or Holzapfel et al (2000, pp 1–48) and references cited therein for a detailed outline. Nevertheless, the characterisation of the (fibre-) morphology of biological tissues remains an elaborate but fundamental task in order to link computational models and in vivo materials; see, for example, the review article by Zysset (2003) and references cited therein, where special emphasis is placed on hard tissues—namely bones. The overall behaviour of commonly considered biological materials is apparently anisotropic, such that concepts from classical continuum mechanics, as highlighted in the contributions in Boehler (1987) and by Spencer (1984), serve as a convenient backbone; see also Weiss et al (1996) and Almeida and Spilker (1998) for the modelling of the anisotropic elastic behaviour of soft tissues and Cowin (1985), Zysset and Curnier (1995), Cowin (1998), and Menzel and Steinmann (2001a) for alternative frameworks. Passive response is however not at all restricted to non-dissipative processes; in other words, anisotropic viscoelastic and anisotropic elastoplastic behaviour occur—see, for example, the formulation by Holzapfel and Gasser (2001) or Kaliske (2000), and the contribution by Gasser and Holzapfel (2003).

In contrast to the viscous behaviour within passive response, one observes that remodelling effects take place on a different, drastically larger, timescale; see

A. Menzel
Chair of Applied Mechanics,
Department of Mechanical and Process Engineering,
University of Kaiserslautern, P.O. Box 3049,
67653 Kaiserslautern, Germany
E-mail: amenzel@rhrk.uni-kl.de
URL: http://mechanik.mv.uni-kl.de

Currey (2003) with application to bones. We will therefore not incorporate viscoelastic constitutive laws into the formulation developed in this contribution, but account for remodelling, namely isotropic and anisotropic growth and reorientation. Keeping, say, a soft tissue in mind, consider an assembly or bundle of collagen fibrils that form fibres; see Silver et al (2003). From a macroscopic point of view, collections of fibres are essentially characterised via a representative diameter and a corresponding orientation or rather direction. Apparently, the direction naturally evolves such that the loading capacity of the in vivo material is optimised (the transcription of this effect in terms of mathematical equations is a non-trivial task); see, for instance, the framework developed in Driessen et al (2003), which is based on probability distributions for fibre directions, the contribution by Sherratt et al (1992) or Menzel and Steinmann (2001b, 2003a, b) as well as Menzel et al (2004), where computational frameworks for inelastic constitutive relations with evolving axes of anisotropy are developed, and references cited therein. Moreover, it is accepted that the fibre diameter increases in response to mechanical stimuli like stress (which means that the diameter is correlated with the strength of the fibre), but that the fibre diameter is also age-dependent. In addition, initially randomly-distributed fibre directions (which can easily be modelled within a numerical setting) that later on adapt according to a particular type of loading path would provide further insight and understanding of the mechanical remodelling process of the in vivo material. Since the temperature of the living tissues considered is almost constant, thermal coupling is usually neglected. However, electric effects and stimuli as well as age dependency should also be addressed—especially for the modelling of muscle contraction; see, for example, Schneck (1992) or Wren (2003) among others. These properties, as well as observations like regeneration after injury or surface growth, as discussed by Skalar et al (1997), are however not within the scope of the present work, where we restrict ourselves to purely mechanical stimuli.

From the continuum mechanics point of view, it is an old but ongoing discussion concerning the adoption of the theory of porous media or the theory of open systems for the modelling of growth phenomena; see, for instance, the early and pioneering contributions by Truesdell and Toupin (1960), Bowen (1976), Cowin and Hegedus (1976), and the survey article by Cowin (1999a) or the monographs by de Groot (1961), Kestin (1966) and Katchalsky and Curran (1965), where detailed background information on the underlying theories are provided. In this contribution, we adopt the latter approach, as further developed in Epstein and Maugin (2000) and Kuhl and Steinmann (2003a, b). Numerical simulations of biological materials, in particular bones, were initiated more than two decades ago, as reviewed by Huiskes and Chao (1983). Stable computational models for the (Wolff-type) adaption of hard tissues, however, were devised in the late 1980s and early 1990s by Huiskes et al (1987), Weinans et al (1992) and Harrigan and Hamilton (1992, 1993, 1994). Based on these isotropic remodelling formulations, several numerical approaches were further elaborated; see Jacobs et al (1995), Nackenhorst (1996), or Kuhl and Steinmann (2003c, 2004), where in contrast to the previously cited references, the incorporation and computational treatment of an additional mass flux term is developed. For a discussion of various aspects of the underlying numerical techniques and a comparison of two different discretisation approaches for the density field, we refer the reader to Kuhl et al (2003).

Since the response and adaptation of biomaterials is usually anisotropic, models for anisotropic growth or anisotropic remodelling were (are) consequently developed. Even though, at first glance, several proposed formulations seem similar to well-established frameworks in computational finite inelasticity, one has to account for the fundamental difference (compared to plasticity for instance) that growth contributes to a transformation which should finally link compatible configurations. Accordingly, it is common practice to introduce an additional (linear tangent) map in order to satisfy this compatibility constraint. The concept of a growth mapping, as typically represented in terms of a corresponding linear tangent map or rather growth tensor, is advocated in the pioneering work by Rodriguez et al (1994), and further discussed and elaborated in Taber (1995) and Cowin (1996) or the recent work by Lubarda and Hoger (2002), among others. Similar concepts are based on so-called remodelling or virtual configurations, which are directly related to the material setting and therefore allow the incorporation of a (local) change of the reference state, as proposed by Chen and Hoger (2000), Ambrosi and Mollica (2002), Imatani and Maugin (2002), Maugin and Imatani (2003a, b) and Garikipati et al (2004). Since the development of these anisotropic growth theories is currently still under discussion, it is not astonishing that these formulations are somehow ahead of the set-up of appropriate computational frameworks. To be specific, most of the pioneering contributions, that address robust algorithms in order to simulate anisotropic remodelling within a finite element setting, are mainly restricted to small strains and hard tissues; compare Jacobs et al (1997), Weng (1998) or Krstin et al (2000).

The main goal and contribution of this work consists in the development of a theoretical and computational framework, which accounts for anisotropic growth under finite deformations. The adopted concept thereby diverges from the previously cited works on anisotropic growth. Practically speaking, we directly introduce an additional internal variable, which allows the anisotropic growth formulation, rather than introducing any additional remodelling configuration. Compatibility constraints of the overall motion are therefore naturally not additionally addressed. The purely isotropic or volumetric growth is conveniently modelled via an (Wolff-type) evolution of the referential density field.

The remaining task apparently consists of the set-up of a physically sound evolution equation for the anisotropic portion of the remodelling process. Following straightforward concepts of computational inelasticity, one usually determines the dual force of the anisotropy variable, defines an appropriate dissipation potential, and ends up with a corresponding (possibly associated) evolution equation; see Menzel and Steinmann (2001b, 2003a, b). The physical interpretation for a biological tissue would nevertheless be questionable in some way. This once again motivates the application of a Wolff-type evolution law, namely an energy-driven format, for the norm of the anisotropy variable. Concerning the remodelling of the anisotropy axes, we adopt ideas that are well-known in the theory of anisotropic elastic solids (undergoing small strains), namely the assumption of coaxial stress and strain fields. To be specific, it has been shown that the strain energy takes an extremum only if the principal stress directions coincide with the principal strain directions—see Petersen (1989), Cowin (1994, 1995, 1997), Vianello (1996a, b) and Sgarra and Vianello (1997) with special emphasis on a finite deformation setting. Moreover, it has also been proven that orthogonal (symmetry) transformations exist, which can be superposed onto the referential constitutive relation and thereby enable the construction of coaxial stress and strain tensors for a generally anisotropic material. Since energy optimisation or rather minimisation is commonly considered to be a basic axiom in nature, these ideas are carried over to the problem at hand. In this context, we must align the anisotropy variable with the strain field such that stress and strains finally commute (note that an alignment of the anisotropy variable with the appropriate stress field generally results in non-commutative stress and strain tensors). For the numerical treatment of this reorientation, it is straightforward to adopt similar algorithms to those applied in viscoelasticity, such that a time-dependent and saturation-type reorientation is obtained. While this concept of an energy extremum holds for homogeneous deformations in general, we are also interested in inhomogeneous boundary value problems where a general proof is not obvious. To give an example, the fibre direction at or even near the surface of a body of interest is usually fixed; for example, perpendicular or parallel to the surface itself. In this work, however, the fibre direction is not constrained by any type of boundary conditions.

The paper is organised as follows: after a brief reiteration of the fundamental balance equations in Sect. 2, the constitutive framework is introduced in Sect. 3. Essential kinematics, as well as the assumed format of the anisotropy variable are pointed out in detail. The main body of the paper consists in the set-up of a prototype model in Sect. 4, where special emphasis is placed on the particular format of the strain energy and the underlying evolution equations. Implicit numerical integration techniques, as well as the overall algorithmic treatment are addressed in Sect. 5. Several numerical examples show the applicability of the proposed framework in Sect. 6, which is documented for homogeneous deformations and inhomogeneous deformations within a non-linear finite element setting. A short summary accompanied by a brief outlook on future research is given in Sect. 7.

2 Balance equations

For the convenience of the reader, and in order to introduce the applied notation, we first summarise some essential kinematics of non-linear continuum mechanics, and then address the underlying balance equations. In this context, let $\boldsymbol{X} \in 1\mathscr{B}_0 \subset \mathbb{E}^3$ denote placements of particles of the body $\mathcal{B}$ in the reference configuration and $\boldsymbol{x} = \varphi(\boldsymbol{X}, t) \in \mathscr{B}_t \subset \mathbb{E}^3$ the corresponding non-linear motion that determines the positions of particles in the spatial configuration. The underlying motion gradient is obtained via $\boldsymbol{F} = \partial_{\boldsymbol{X}} \varphi$. For a detailed outline, we refer the reader to the monographs by Liu (2002), Haupt (2000) or Holzapfel (2000).

Next, let ρ_0 characterise the referential density of the body $\mathcal{B}$ at $\boldsymbol{X}$. Balancing this scalar-valued field introduces the mass flux $\boldsymbol{R}$ and the mass source term R_0, namely

$$\mathrm{D}_t \rho_0 = \nabla_{\boldsymbol{X}} \cdot \boldsymbol{R} + R_0 \tag{1}$$

whereby the notation D_t abbreviates the material time derivative. For conceptual simplicity, we neglect the flux term in the sequel, $\boldsymbol{R} \doteq \boldsymbol{0}$, such that $\mathrm{D}_t \rho_0 \doteq R_0$, which however does not restrict the proposed constitutive framework itself. Nevertheless, it is of cardinal importance for the progression of this work on open systems that the source term does not vanish as for the standard mass-conservation approach, which has been denoted as the passive response in the introduction. Eq. 1 apparently represents isotropic or rather volumetric growth of the considered biomaterial. It is therefore obvious that with the mass being a non-conserved quantity, different (non-standard) representations of the commonly considered balance laws are obtained. Based on the assumed representation of the mass-balance, we observe for instance, that an analogous balance relation for linear momentum ($\rho_0 \mathrm{D}_t \phi$) now reads

$$\mathrm{D}_t(\rho_0 \mathrm{D}_t \varphi) = \nabla_{\boldsymbol{X}} \cdot \boldsymbol{\Pi}^{\mathrm{t}} + \boldsymbol{b}_0 + R_0 \mathrm{D}_t \varphi \tag{2}$$

with $\boldsymbol{\Pi}^{\mathrm{t}}$ and $\boldsymbol{b}_0 + R_0 \mathrm{D}_t \varphi$ denoting the momentum flux (first Piola–Kirchhoff stress) and source, respectively. We similarly obtain the correlation

$$\mathrm{D}_t(\rho_0\, \varepsilon) = \boldsymbol{\Pi}^{\mathrm{t}} : \mathrm{D}_t \boldsymbol{F} - \nabla_{\boldsymbol{X}} \cdot \boldsymbol{Q} + Q_0 + R_0 \varepsilon \tag{3}$$

for the balance of internal energy ($\rho_0 \epsilon$), whereby $-\boldsymbol{Q}$ represents the flux of non-mechanical energy and $Q_0 + R_0 \varepsilon$ characterises the non-mechanical source term. Furthermore, the balance of entropy ($\rho_0\, \eta$) is denoted as

$$\mathrm{D}_t(\rho_0\, \eta) = -\nabla_{\boldsymbol{X}} \cdot \boldsymbol{H} + H_0 + R_0 \eta + \gamma_0 \tag{4}$$

with $-\boldsymbol{H}$ and $H_0 + R_0\, \eta$ denoting the entropy flux and source whereas $\gamma_0 \geq 0$ abbreviates the entropy production. Next, by introducing the absolute temperature $\theta > 0$ such

that the volume specific free Helmholtz energy takes the format $\psi \doteq \varepsilon - \theta\eta$, we obtain, after some straightforward transformations, the well-established Clausius–Duhem inequality as

$$\begin{aligned}\theta\gamma_0 = \boldsymbol{\Pi}^{\mathrm{t}} : \mathrm{D}_t\boldsymbol{F} - \rho_0\mathrm{D}_t\psi - \rho_0\eta\mathrm{D}_t\theta - \theta\Gamma_0 \\ - \theta^{-1}\boldsymbol{Q}\cdot[\nabla_{\boldsymbol{X}}\otimes\theta] \geqslant 0.\end{aligned} \tag{5}$$

Thereby the relations $\boldsymbol{H} \doteq \theta^{-1}\boldsymbol{Q}$ as well as $H_0 \doteq \theta^{-1}Q_0 + \Gamma_0$, respectively, have been assumed and the connection $\psi\mathrm{D}_t\rho_0 = R_0\epsilon - \theta R_0\eta$ stems from the incorporated version of the balance of mass. In fact, the additional term Γ_0, which is additively decomposed into $\Gamma_0 \doteq {}^{\rho_0}\Gamma_0 + {}^{\lambda^A}\Gamma_0 + {}^{n^A}\Gamma_0$ as this work progresses, accounts for the entropy supply caused by the ambient material of the considered particle or rather local chart.

3 Constitutive framework

In this contribution, we develop a framework for modelling the adaptation of soft tissues—typically ligaments, tendons, different types of muscles, skin, vessels as, for example, arteries, and so on (the same framework can however also be applied to hard tissues, such as bones, without loss of generality). It is therefore obvious that the timescale considered for the underlying remodelling process is far beyond those commonly taken into account for the formulation of visco- and thermoelastic or inertia effects. In what follows, we adopt the viewpoint that any applied load or boundary condition represents an assembly of driving effects averaged over time.

In this context, let the free Helmholtz energy be a function of the absolute temperature θ, the referential density ρ_0, the deformation gradient $\boldsymbol{F}$ and an additional vector, say $\boldsymbol{a} \in \mathscr{B}_0$, whose direction characterises a fibre of the considered body and so defines the underlying material symmetry class, namely transversal isotropy. With these arguments in hand, it is the principle of invariance under superposed rigid body motions in combination with the dependency of the response functions on the direction of $\boldsymbol{a}$ (but not the orientation of $\boldsymbol{a}$) that imposes the following representation

$$\psi = \psi(\theta,\, \rho_0,\, \boldsymbol{F},\, \boldsymbol{a};\, \boldsymbol{X}) \doteq \psi(\theta,\, \rho_0,\, \boldsymbol{C},\, \boldsymbol{A};\, \boldsymbol{X}) \tag{6}$$

whereby the right Cauchy–Green tensor $\boldsymbol{C}$ and a (sign-independent) symmetric rank one structural tensor $\boldsymbol{A}$ have been introduced

$$\begin{aligned}&\boldsymbol{C} = \boldsymbol{F}^{\mathrm{t}}\cdot\boldsymbol{F} = \sum_{i=1}^{3}\lambda_i^C\boldsymbol{n}_i^C\otimes\boldsymbol{n}_i^C,\\ &\boldsymbol{A} = \boldsymbol{a}\otimes\boldsymbol{a} = \lambda^A\boldsymbol{n}^A\otimes\boldsymbol{n}^A,\\ &\text{with}\quad \boldsymbol{n}_i^C\cdot\boldsymbol{n}_j^C = \delta_{ij},\quad \boldsymbol{n}^A\cdot\boldsymbol{n}^A = 1,\\ &\lambda^A = \boldsymbol{a}\cdot\boldsymbol{a},\quad \lambda_i^C|_{t_0} = \lambda^A|_{t_0} \doteq 1.\end{aligned} \tag{7}$$

Conceptually speaking, λ^A herein denotes the norm of the structural tensor or the fibre diameter to the power of two, and the fibre direction is characterised by the (sign-independent) contribution $\boldsymbol{n}^A\otimes\boldsymbol{n}^A$. Since ψ is assumed to represent an isotropic tensor function with respect to its arguments, we consequently obtain a set of 12 scalar-valued functions, which determine the free Helmholtz energy

$$\begin{aligned}&\theta,\, \rho_0,\, I_i = \boldsymbol{I} : \boldsymbol{C}^i,\\ &I_{i+3} = \boldsymbol{I} : \boldsymbol{A}^i = [\lambda^A]^i \quad \text{for} \quad i = 1,\, 2,\, 3,\\ &I_7 = \boldsymbol{C} : \boldsymbol{A},\; I_8 = \boldsymbol{C} : [\boldsymbol{A}\cdot\boldsymbol{C}],\\ &I_9 = \boldsymbol{A} : [\boldsymbol{C}\cdot\boldsymbol{A}],\quad I_{10} = \boldsymbol{C} : [\boldsymbol{A}\cdot\boldsymbol{C}\cdot\boldsymbol{A}];\end{aligned} \tag{8}$$

note that $\boldsymbol{I}$ denotes the second order material identity and that $\boldsymbol{A}$ is not restricted to remaining constant during a deformation process.

Based on these arguments, the dissipation inequality as highlighted in Eq. 5 reads

$$\begin{aligned}\theta\gamma_0 = [\boldsymbol{\Pi}^{\mathrm{t}} - \rho_0\partial_{\boldsymbol{F}}\psi] : \mathrm{D}_t\boldsymbol{F} - [\rho_0\eta + \rho_0\partial_\theta\psi]\mathrm{D}_t\theta \\ - \rho_0\partial_{\rho_0}\psi R_0 - \rho_0\partial_{\boldsymbol{A}}\psi : \mathrm{D}_t\boldsymbol{A} \\ - \theta[{}^{\rho_0}\Gamma_0 + {}^{\lambda^A}\Gamma_0 + {}^{n^A}\Gamma_0] - \theta^{-1}\boldsymbol{Q}\cdot[\nabla_{\boldsymbol{X}}\otimes\theta] \geqslant 0\end{aligned} \tag{9}$$

and, adopting the standard argumentation of rational thermodynamics, we introduce the hyperelastic formats

$$\begin{aligned}&[\boldsymbol{\Pi}^{\mathrm{t}} - \rho_0\partial_{\boldsymbol{F}}\psi] \doteq \boldsymbol{0} \rightarrow \boldsymbol{\Pi}^{\mathrm{t}} = \rho_0\partial_{\boldsymbol{F}}\psi,\\ &[\rho_0\eta + \rho_0\partial_\theta\psi] \doteq 0 \rightarrow \eta \doteq -\partial_\theta\psi.\end{aligned} \tag{10}$$

From the list of tensorial arguments that enter the free Helmholtz energy, namely $\boldsymbol{C}(\boldsymbol{F})$ and $\boldsymbol{A}(\lambda^A, \boldsymbol{n}^A)$, we first observe the well-established relation

$$\partial_{\boldsymbol{F}}\psi = \partial_{\boldsymbol{C}}\psi : \partial_{\boldsymbol{F}}\boldsymbol{C} = 2\boldsymbol{F}\cdot\partial_{\boldsymbol{C}}\psi, \tag{11}$$

whereby use of the symmetry of $\partial_{\boldsymbol{C}}\psi$ has been made. This representation suggests the introduction of a symmetric stress tensor (second Piola–Kirchhoff), and allows the convenient set-up of a spectral decomposition

$$\boldsymbol{F}^{-1}\cdot\boldsymbol{\Pi}^{\mathrm{t}} = 2\rho_0\partial_{\boldsymbol{C}}\psi \doteq \boldsymbol{S} = \sum_{i=1}^{3}\lambda_i^S\boldsymbol{n}_i^S\otimes\boldsymbol{n}_i^S,\quad \boldsymbol{n}_i^S\cdot\boldsymbol{n}_j^S = \delta_{ij}. \tag{12}$$

Moreover, its energetically conjugate or rather dual field takes the well-known format $\frac{1}{2}[\boldsymbol{F}^{\mathrm{t}}\cdot\mathrm{D}_t\boldsymbol{F}]^{\mathrm{sym}} = \frac{1}{2}\mathrm{D}_t\boldsymbol{C}$. The second remaining contribution in Eq. 9, which refers to the structural tensor, may be rewritten as

$$\begin{aligned}&-\rho_0\partial_{\boldsymbol{A}}\psi : \mathrm{D}_t\boldsymbol{A} \rightarrow -\rho_0\partial_{\lambda^A}\psi\mathrm{D}_t\lambda^A - \rho_0\partial_{\boldsymbol{n}^A}\psi\cdot\mathrm{D}_t\boldsymbol{n}^A\\ &\text{with}\quad \partial_{\lambda^A}\psi = \partial_{\boldsymbol{A}}\psi : [\boldsymbol{n}^A\otimes\boldsymbol{n}^A],\\ &\qquad \partial_{\boldsymbol{n}^A}\psi = 2\lambda^A\partial_{\boldsymbol{A}}\psi\cdot\boldsymbol{n}^A.\end{aligned} \tag{13}$$

With these relations in hand, the dissipation inequality Eq. 9 allows representation in terms of the reduced format

$$\begin{aligned}\theta\gamma_0^{\mathrm{red}} &= \theta\big[-{}^{\rho_0}\Gamma_0 - \theta^{-1}\rho_0\partial_{\rho_0}\psi R_0\big]\\ &\quad+\theta\Big[-{}^{\lambda^A}\Gamma_0 - \theta^{-1}\rho_0\partial_{\boldsymbol{A}}\psi : [\boldsymbol{n}^A\otimes\boldsymbol{n}^A]\mathrm{D}_t\lambda^A\Big]\\ &\quad+\theta\Big[-{}^{n^A}\Gamma_0 - 2\theta^{-1}\rho_0\lambda^A\boldsymbol{n}^A\cdot\partial_{\boldsymbol{A}}\psi\cdot\mathrm{D}_t\boldsymbol{n}^A\Big]\\ &\quad+\theta\big[-\theta^{-2}\boldsymbol{Q}\cdot[\nabla_{\boldsymbol{X}}\otimes\theta]\big]\\ &\doteq\theta\Big[{}^{\rho_0}\gamma_0+{}^{\lambda^A}\gamma_0+{}^{n^A}\gamma_0+{}^{\theta}\gamma_0\Big]\geqslant 0.\end{aligned}\tag{14}$$

For the course of this work, we adopt the commonly applied (reduced) ansatz that each individual contribution is non-negative, so that ${}^{\rho_0}\gamma_0, {}^{\lambda^A}\gamma_0, {}^{n^A}\gamma_0, {}^{\theta}\gamma_0\geqslant 0$ whereby $\theta^2\,{}^{\theta}\gamma_0\geqslant 0$ is established as Fourier's inequality. Conceptually speaking, the entropy supply terms ${}^{\rho_0}\Gamma_0, {}^{\lambda^A}\Gamma_0$ and ${}^{n^A}\Gamma_0$ compensate for stiffening and remodelling effects of the biomaterial due to isotropic growth ($\mathrm{D}_t\rho_0\neq 0$), growth of the fibre diameter ($\mathrm{D}_t\lambda^A\neq 0$) and fibre reorientation ($\mathrm{D}_t\boldsymbol{n}^A\neq\boldsymbol{0}$), respectively.

4 Prototype model

For the subsequent prototype model, as well as for the subsequent numerical examples, we restrict ourselves to an isothermal setting, so that $\theta\doteq\text{const}\rightarrow\nabla_{\boldsymbol{X}}\otimes\theta=\boldsymbol{0}$, and consequently ${}^{\theta}\gamma_0=0$ which allows us to cancel out the temperature field from the list of arguments that enter the free Helmholtz energy. In the following, the commonly applied additive split of the free Helmholtz energy into a purely isotropic contribution and an additional anisotropic part is adopted. Moreover, the referential density is assumed to weight the free Helmholtz energy via

$$\begin{aligned}&\psi(\rho_0,\boldsymbol{C}(\boldsymbol{F}),\boldsymbol{A}(\lambda^A,\boldsymbol{n}^A);\boldsymbol{X})\\ &\quad\doteq\left[\frac{\rho_0}{\rho_0^*}\right]^n\big[\psi^{\mathrm{iso}}(\rho_0,\boldsymbol{C};\boldsymbol{X})+\psi^{\mathrm{ani}}(\rho_0,\boldsymbol{C},\boldsymbol{A};\boldsymbol{X})\big]\end{aligned}\tag{15}$$

with $1\leq n\leq 3.5$, which is a well-established ansatz, whereby $\rho_0{}^*>0$ denotes some fixed initial value for the density field. We choose in particular

$$\begin{aligned}\rho_0\psi^{\mathrm{nh}}&\doteq\frac{\mu}{2}[I_1-3],\\ \rho_0\psi^{\mathrm{iso}}&\doteq\rho_0\psi^{\mathrm{nh}}-\mu\ln(J)+\frac{\lambda}{2}\ln^2(J),\\ \rho_0\psi^{\mathrm{ani}}&\doteq\frac{\alpha}{2\beta}\Big[\exp(\beta[I_7-I_4]^2)-1\Big],\end{aligned}\tag{16}$$

with $\lambda,\mu,\alpha,\beta,J>0$ as well as $J=\det(\boldsymbol{F})=\big[\frac{1}{3}I_3-\frac{1}{2}I_1I_2+\frac{1}{6}I_1^3\big]^{1/2}$. The anisotropic contribution has been adopted in analogy to Holzapfel et al (2000), see also remark 1. Setting up appropriate evolution equations for the referential density ρ_0 and the structural tensor in terms of λ^A and $\boldsymbol{n}^A$, respectively, remains to be completed.

4.1 Referential density evolution

Concerning the evolution of the density field, it has been proven by Harrigan and Hamilton (1992, 1993, 1994) that the evolution equation

$$\mathrm{D}_t\rho_0=R_0\doteq[1-q_{\rho_0}]\left[\left[\frac{\rho_0}{\rho_0^*}\right]^{-m}\rho_0\psi-{}^{\rho_0}\psi_0^*\right]\tag{17}$$

for the referential density guarantees (for an isotropic and small strain setting) existence and uniqueness of a global minimum of the stored energy if $m>n$, see also remark 5, whereby ${}^{\rho_0}\psi_0^*>0$ denotes a fixed initial value for the free Helmholtz energy or rather density stimulus and $q_{\rho_0}\in[0,1]$ is a constant scaling factor. When choosing the ansatz ${}^{\rho_0}\Gamma_0\doteq\theta^{-1}[1-n]\psi R_0$ for the extra entropy supply, we observe that the density contribution to the dissipation inequality as highlighted in Eq. 14 disappears, namely ${}^{\rho_0}\gamma_0=-{}^{\rho_0}\Gamma_0-\theta^{-1}\rho_0\partial_{\rho_0}\psi R_0=-{}^{\rho_0}\Gamma_0+\theta^{-1}[1-n]\psi R_0=0$. Practically speaking, any ${}^{\rho_0}\Gamma_0\lesseqgtr-\theta^{-1}\rho_0\partial_{\rho_0}\psi R_0$ satisfies this particular fraction of the dissipation inequality; in other words ${}^{\rho_0}\gamma_0\geqslant 0$.

4.2 Fibre strength evolution

In analogy to the density contribution, we now introduce a constitutive equation for the length, diameter or the strength of the fibre $\boldsymbol{a}$, respectively, which is directly related to the norm of the structural tensor $\boldsymbol{A}$, in other words λ^A. It is therefore obvious that an increase of λ^A stiffens the material, while decreasing λ^A characterises degradation. In order to set up an "energy-driven" evolution equation, we define the projected right Cauchy-Green tensor

$$\begin{aligned}{}^A\boldsymbol{C}&\doteq\boldsymbol{I}+[\boldsymbol{n}^A\cdot\boldsymbol{C}\cdot\boldsymbol{n}^A-1]\boldsymbol{n}^A\otimes\boldsymbol{n}^A\\ &=\boldsymbol{I}+\Big[[\lambda^A]^{-1}I_7-1\Big]\boldsymbol{n}^A\otimes\boldsymbol{n}^A\end{aligned}\tag{18}$$

which accounts solely for the stretch (to the power of two) along the direction of the fibre, and determines a modified Neo–Hookean contribution ${}^A\psi^{\mathrm{nh}}(\rho_0,{}^A\boldsymbol{C};\boldsymbol{X})$ in the sequel. Based on this projected kinematic field, we choose

$$\begin{aligned}\mathrm{D}_t\lambda^A\doteq[1-q_{\lambda^A}]&\left[\left[\frac{\alpha}{2\beta}\exp(\beta[I_7-I_4]^2)+\frac{\mu}{2}I_7\right]^{-l}\right.\\ &\left.\times\left[\frac{\rho_0}{\rho_0^*}\right]^n\rho_0[{}^A\psi^{\mathrm{nh}}+\psi^{\mathrm{ani}}]-{}^{\lambda^A}\psi_0^*\right]\end{aligned}\tag{19}$$

with $l>1$, see remark 5, and the constant scaling factor $q_{\lambda^A}\in[0,1]$. Adopting the previously applied approach once more, one obtains from ${}^{\lambda^A}\Gamma_0\doteq-2\beta\theta^{-1}\rho_0I_4^{-1}[I_7-I_4]^2[\rho_0/\rho_0^*]^n[\psi^{\mathrm{ani}}+1]\mathrm{D}_t\lambda^A$, a vanishing contribution of λ^A to the dissipation inequality in Eq. 14, in other words ${}^{\lambda^A}\gamma_0=-{}^{\lambda^A}\Gamma_0-\theta^{-1}\rho_0\partial_{\boldsymbol{A}}\psi:[\boldsymbol{n}^A\otimes\boldsymbol{n}^A]\mathrm{D}_t\lambda^A=0;;$ see also Eq. 23 below for the derivation of this particular ansatz. Nevertheless, any ${}^{\lambda^A}\Gamma_0\lesseqgtr-\theta^{-1}\rho_0\partial_{\boldsymbol{A}}\psi:[\boldsymbol{n}^A\otimes\boldsymbol{n}^A]\mathrm{D}_t\lambda^A$ apparently guarantees ${}^{\lambda^A}\gamma_0\geqslant 0$.

4.3 Fibre direction evolution

Finally, emphasis is placed on the evolution of the fibre direction of the material, which is characterised by the unit vector $\boldsymbol{n}^A$. Due to the nature of elements of unit spheres, the evolution boils down to a rotation and the correlated velocity allows representation as

$$\mathrm{D}_t \boldsymbol{n}^A = \boldsymbol{\omega} \times \boldsymbol{n}^A = [-\boldsymbol{\varepsilon} \cdot \boldsymbol{\omega}] \cdot \boldsymbol{n}^A \tag{20}$$

whereby $\boldsymbol{\omega}$ and $\boldsymbol{\varepsilon}$ denote the underlying angular velocity and the permutation tensor of third order, respectively. For a small strain setting, it has been shown that the stored energy takes an extremum if the principal stress directions coincide with the principal strain directions; see the references cited in the introduction. In this context, we observe that the symmetric stress tensor as introduced in Eq. 12 takes the general representation

$$\begin{aligned}\boldsymbol{S} = 2\rho_0 [&S_1 \boldsymbol{I} + 2S_2 \boldsymbol{C} + 3S_3 \boldsymbol{C}^2 + S_7 \boldsymbol{A} + 2S_8 [\boldsymbol{A} \cdot \boldsymbol{C}]^{\mathrm{sym}} \\ &+ S_9 \boldsymbol{A}^2 + 2S_{10} \boldsymbol{A} \cdot \boldsymbol{C} \cdot \boldsymbol{A}]\end{aligned} \tag{21}$$

for the problem at hand, whereby the scalars $S_{1,2,3,7,\ldots,10}$ are functions of the scalar-valued fields and polynomial invariants highlighted in Eq. 8. It is therefore obvious that appropriate stress and stretch or rather strain fields commute if the anisotropy axis $\boldsymbol{a}$ shares its direction with one of the principal strain directions. This motivates the alignment of the fibre vector $\boldsymbol{n}^A$ with the eigenvector $\boldsymbol{n}_3{}^C$ of the right Cauchy–Green tensor, with $\lambda_1{}^C \leq \lambda_2{}^C \leq \lambda_3{}^C$. We consequently choose

$$\begin{aligned}&\boldsymbol{\omega} \doteq [1 - q_{\boldsymbol{n}^A}] \frac{\pi}{2t^*} \boldsymbol{n}^A \times \boldsymbol{n}_3^C \\ &\quad \left(\text{and if } \boldsymbol{n}^A \cdot \boldsymbol{n}_3^C < 0 \text{ then } -\boldsymbol{n}_3^C \mapsto \boldsymbol{n}_3^C\right)\end{aligned} \tag{22}$$

whereby $t^* > 0$ acts in a similar way to a relaxation time parameter in viscoelasticity and the interval of the constant scaling factor $q_{\boldsymbol{n}^A} \in [0, 1]$ being obvious (recall that the considered eigenvectors are independent of sign); see also remark 4 in this context. For equal eigenvalues, in other words $\lambda_1{}^C < \lambda_2{}^C = \lambda_3{}^C$ or $\lambda_1{}^C = \lambda_2{}^C = \lambda_3{}^C$ (but not $\lambda_1{}^C = \lambda_2{}^C < \lambda_3{}^C$), any evolution of the fibre direction is neglected by simply setting $\mathrm{D}_t \boldsymbol{n}^A \doteq \boldsymbol{0}$. Concerning the dissipation inequality, we first compute the derivative

$$\partial_{\boldsymbol{A}} \psi = 2\beta [I_7 - I_4] \left[\frac{\rho_0}{\rho_0^*}\right]^n [\psi^{\mathrm{ani}} + 1][\boldsymbol{C} - \boldsymbol{I}] \tag{23}$$

and then observe from $\boldsymbol{n}^A \cdot \mathrm{D}_t \boldsymbol{n}^A = 0$ that the assumption ${}^{n^A}\Gamma_0 \doteq -4\lambda^A \beta \theta^{-1} \rho_0 [\rho_0 / \rho_0^*]^n [I_7 - I_4][\psi^{\mathrm{ani}} + 1] \boldsymbol{n}^A \cdot \boldsymbol{C} \cdot \mathrm{D}_t \boldsymbol{n}_A$ results in ${}^{n^A}\gamma_0 = -{}^{n^A}\Gamma_0 - 2\theta^{-1} \rho_0 \lambda^A \boldsymbol{n}^A \cdot \partial_{\boldsymbol{A}} \psi \cdot \mathrm{D}_t \boldsymbol{n}_A = 0$. However, any choice with ${}^{n^A}\Gamma_0 \leqslant -2\theta^{-1} \rho_0 \lambda^A \boldsymbol{n}^A \cdot \partial_{\boldsymbol{A}} \psi \cdot D_t \boldsymbol{n}_A$ satisfies the reorientation part in the dissipation inequality, as highlighted in Eq. 14.

Remark 1 The anisotropic part of the chosen free Helmholtz energy, as highlighted in Eq. 16, incorporates the difference of the invariants I_7 (trace of the product of the right Cauchy–Green tensor and the structural tensor) and I_4 (trace of the structural tensor). The incorporation of I_4 instead of some constant value, typically one as applied in Holzapfel et al (2000), stems from the fact that the structural tensor itself is not constant for the proposed framework. The assumed format apparently guarantees a stress free setting after unloading since $I_7 \rightarrow I_4$ for $\boldsymbol{F} \rightarrow \boldsymbol{I}$. However, if I_4 is replaced, for instance, by the constant $I_4|_{t_0}$ one might end up with a convenient model that allows the formulation of residual stresses stemming from the remodelling of the fibres (softening and strengthening); see also the outlook in the Sect. 7.3.1.

Remark 2 The anisotropic contribution of the chosen format for the free Helmholtz energy in Eq. 16 cannot (as yet) be proven to fulfil the condition of polyconvexity; see Ball (1977), Ciarlet (1988) and Šilhavý (1997) or Dacorogna (1989) and Giusti (2003) for general surveys. The specific case with $\boldsymbol{a} = \text{const}$ and $\lambda^A = 1$ is discussed by Schröder and Neff (2003); see also the discussion on convexity and material stability in the contribution in Holzapfel and Ogden (2003, pp 65–108) and Merodio and Ogden (2003). To the knowledge of the author, however, there is no analysis available to date (and moreover not in the focus of this work) that provides polyconvex functions within the present context, in other words $\lambda^A \neq \text{const}$ and $\boldsymbol{n}^A \neq \text{const}$. In view of the application of relaxation techniques to the problem at hand we refer the reader to Conti et al (2002) or Dolzmann (2003) and references cited therein.

Remark 3 The computation of a symmetric spatial stress field that enters the balance of linear momentum is straightforward and based directly on the pushforward of the stress tensor highlighted in Eq. 21. In this context, the Cauchy stress tensor $\boldsymbol{\sigma} = J^{-1} \boldsymbol{F} \cdot \boldsymbol{S} \cdot \boldsymbol{F}^{\mathrm{t}}$ reads

$$\begin{aligned}\boldsymbol{\sigma} = 2\rho_0 J^{-1} [&S_1 \boldsymbol{b} + 2S_2 \boldsymbol{b}^2 + 3S_3 \boldsymbol{b}^3 + S_7 \boldsymbol{\alpha} + 2S_8 [\boldsymbol{\alpha} \cdot \boldsymbol{b}]^{\mathrm{sym}} \\ &+ S_9 \boldsymbol{\alpha} \cdot \boldsymbol{b}^{-1} \cdot \boldsymbol{\alpha} + 2S_{10} \boldsymbol{\alpha}^2]\end{aligned} \tag{24}$$

whereby $\boldsymbol{b} = \boldsymbol{F} \cdot \boldsymbol{F}^{\mathrm{t}}$ denotes the Finger tensor and the abbreviation $\boldsymbol{\alpha} = \boldsymbol{F} \cdot \boldsymbol{A} \cdot \boldsymbol{F}^{\mathrm{t}} \doteq \lambda^\alpha \boldsymbol{n}^\alpha \otimes \boldsymbol{n}^\alpha$, with $\boldsymbol{n}^\alpha \cdot \boldsymbol{n}^\alpha = 1$ such that $\lambda^\alpha = \lambda^A$ $\boldsymbol{n}^A \cdot \boldsymbol{C} \cdot \boldsymbol{n}^A = I_7$, has been applied; for a detailed outline on the formulation of anisotropic hyperelasticity with respect to the spatial setting, we refer the reader to Menzel and Steinmann (2003c).

Remark 4 An alternative but reduced ansatz for the anisotropic constitutive equation is based on the idea that appropriate stress and strain fields commute during the entire deformation process. The corresponding universal representation then reads

$$\boldsymbol{S} \doteq 2\rho_0 \sum_{i=1}^{3} s_i \boldsymbol{C}^{i-1}, \quad \boldsymbol{\sigma} \doteq 2\rho_0 J^{-1} \sum_{i=1}^{3} s_i \boldsymbol{b}^i, \tag{25}$$

see Beatty (1987) or Imatani and Maugin (2002) with application to isotropic elasticity and anisotropic growth, respectively. The scalars s_i remain functions of

the scalar-valued fields in Eq. 8. The assumed type of evolution Eq. 22 apparently results for $t \nearrow \infty$ in a formulation that can be boiled down to the representation in Eq. 25.

Remark 5 The Wolff-type law, as highlighted in Eq. 17, guarantees a saturation-type evolution of the density field for $m > n$. Practically speaking, the rate of the referential density (the mass source term) must vanish at a biological equilibrium state. Since $\rho_0\psi$ embodies the referential density to the power of n, see Eq. 15, it is obvious that the saturation effect sought can only be obtained by scaling $\rho_0\,\psi$ with ρ_0 to the power of a factor which is smaller than $-n$, in other words $m > n$; recall that ${}^{\rho_0}\psi_0^* = \text{const}$. Even though the particular representation of the evolution of λ^A looks rather lengthy at first glance, it is the same concept as for the density adopted in Eq. 19 and thereby, the range of the exponent l is also restricted.

Moreover, the assumed evolution type for ρ_0 and λ^A is very convenient on the one hand but also elementary on the other hand since a simple difference relation serves as the basic connection between the correlated driving forces and (constant) stimuli. The incorporation of so-called dead zones, however, is frequently applied in the literature and naturally extends the proposed framework. In addition, a different remodelling response for an increasing/decreasing density field or tension/compression loading of the fibres, respectively, can be modelled—a particular ansatz being the case where fibres under compression are not considered by simply setting $\mathrm{D}_t\,\lambda^A \doteq 0$, $\mathrm{D}_t\boldsymbol{n}^A \doteq \boldsymbol{0}$ or even $\lambda^A \doteq 0$ if $\lambda_3{}^C < 1$ or $\lambda_3{}^S < 0$, respectively; see Reese et al (2001) or De Hart et al (2004) for a similar approach. Since the incorporation of these additional enhancements and constraints is somehow straightforward, we do not focus on these side aspects in the present work.

Remark 6 The orthogonality of $\mathrm{D}_t\boldsymbol{n}^A$ and $\boldsymbol{n}^A$ is clearly monitored by applying the '$\varepsilon\delta$-rule' with respect to Eqs. 20, 22, which results in

$$\mathrm{D}_t\boldsymbol{n}^A \doteq [1 - q_{\boldsymbol{n}^A}]\,\frac{\pi}{2t^*}\left[\boldsymbol{n}_3^C - \left[\boldsymbol{n}_3^C \cdot \boldsymbol{n}^A\right]\boldsymbol{n}^A\right] \;\rightarrow\; \mathrm{D}_t\boldsymbol{n}^A \cdot \boldsymbol{n}^A = 0. \tag{26}$$

An alternative format is provided if one aligns the fibre vector $\boldsymbol{n}^A$ with the principal stress direction $\boldsymbol{n}^S{}_3$ instead of $\boldsymbol{n}^C{}_3$. Indeed, appropriate stress and strain fields in general no longer commute for this ansatz (even for $t \nearrow \infty$).

Remark 7 As previously mentioned in the introduction, standard formulations in computational inelasticity are commonly based on internal variables, which are driven by their dual forces. In this context, the driving force of the structural tensor is determined by Eq. 23 for the problem at hand, see for instance Menzel and Steinmann (2003b) for a comprehensive discussion in the context of anisotropic multiplicative elastoplasticity. We however chose an alternative approach in this work, which enabled us to separately address the evolution of anisotropic growth in terms of fibre strengthening and reorientation.

5 Constitutive integrator

Implicit integration schemes are applied throughout whereby the simple Euler backward rule serves for the density ρ_0 as well as for λ^A, while the set-up of an exponential integration scheme enables us to obtain the classical Euler–Rodrigues formula for the rotation of the direction $\boldsymbol{n}^A$; for an overview, refer to the textbook by Ascher and Petzold (1998) as well as Angeles (1988) and references cited therein.

5.1 Implicit integration techniques

Let the considered time interval of interest be divided into several subintervals $\mathbb{T} = \bigcup_{k=0}^{K}[t_k, t_{k+1}]$ with $\Delta t \doteq t_{k+1} - t_k > 0$ being obvious. The Euler backward scheme applied to the density field now yields

$$\begin{aligned} \rho_0 &= \rho_{0k} + [1 - q_{\rho_0}]\Delta t \quad \left[\left[\tfrac{\rho_0}{\rho_0^*}\right]^{-m}\rho_0\psi \quad -{}^{\rho_0}\psi_0^*\right] \\ &= \rho_{0k} + [1 - q_{\rho_0}]\Delta t \quad \left[{}^{\rho_0}\psi_0 \quad -{}^{\rho_0}\psi_0^*\right] \end{aligned} \tag{27}$$

or rather

$$\begin{aligned} \xi &= \xi_k + \left[1 - q_{\rho_0}\right]\Delta t \quad \left[\xi^{1-m}\psi \quad -\tfrac{1}{\rho_0^*}\rho_0\,\psi_0^*\right] \\ &= \xi_k + \left[1 - q_{\rho_0}\right]\Delta t \quad \left[\xi^{1+n-m}\left[\psi^{\mathrm{iso}} + \psi^{\mathrm{ani}}\right] \quad -\tfrac{1}{\rho_0^*}\rho_0\,\psi_0^*\right] \end{aligned} \tag{28}$$

with $\xi \doteq \rho_0\,/\rho_0{}^*$ denoting the, say, (referential) relative density. The additional index $k+1$ has been neglected; in other words non-indexed ("time-dependent") fields commonly refer to the actual state t_{k+1} in the subsequent algorithmic setting. Concerning the integration of λ^A, we consequently obtain

$$\begin{aligned} \lambda^A &= \lambda_k^A + \left[1 - q_{\lambda^A}\right]\Delta t \\ &\quad \times \left[\left[\tfrac{\alpha}{2\beta}\exp(\beta[I_7 - I_4]^2) + \tfrac{\mu}{2}I_7\right]^{-l}\xi^n\rho_0\left[{}^A\psi^{\mathrm{nh}} + \psi^{\mathrm{ani}}\right] - {}^{\lambda^A}\psi_0^*\right] \\ &= \lambda_k^A + \left[1 - q_{\lambda^A}\right]\Delta t \\ &\quad \times \left[{}^{\lambda^A}\psi_0 \quad -{}^{\lambda^A}\psi_0^*\right]. \end{aligned} \tag{29}$$

As previously mentioned, the integration for $\boldsymbol{n}^A$ is performed by an exponential scheme, namely

$$\boldsymbol{n}^A = \exp(-\Delta t\boldsymbol{\varepsilon} \cdot \boldsymbol{\omega}) \cdot \boldsymbol{n}_k^A = \boldsymbol{R}(\Delta t\boldsymbol{\omega}) \cdot \boldsymbol{n}_k^A \tag{30}$$

where the proper orthogonal tensor $\boldsymbol{R}$ possesses a closed form representation, taking, for example, the format

$$\boldsymbol{R}(\Delta t\omega\boldsymbol{n}^{\omega}) = \cos(\Delta t\omega)\boldsymbol{I} + [1-\cos(\Delta t\omega)]\boldsymbol{n}^{\omega}\otimes\boldsymbol{n}^{\omega} - \sin(\Delta t\omega)\boldsymbol{\varepsilon}\cdot\boldsymbol{n}^{\omega} \tag{31}$$

with $\boldsymbol{\omega}=\omega\boldsymbol{n}^{\omega}$ and $\boldsymbol{n}^{\omega}\cdot\boldsymbol{n}^{\omega}=1$ being obvious. Alternatively, the rotated vector can be directly written as

$$\boldsymbol{n}^{A} = \cos(\Delta t\omega)\boldsymbol{n}_k^{A} + [1-\cos(\Delta t\omega)][\boldsymbol{n}^{\omega}\cdot\boldsymbol{n}_k^{A}]\boldsymbol{n}^{\omega} + \sin(\Delta t\omega)\boldsymbol{n}^{\omega}\times\boldsymbol{n}_k^{A}. \tag{32}$$

5.2 Algorithmic tangent operators

Based on the previously advocated integration techniques, we obtain a system of non-linear equations typically solved via a Newton-type algorithm. The residual format of Eqs. 28, 29, 32 consequently reads

$$\begin{aligned}
r_{\xi} &= \xi-\xi_k-\left[1-q_{\rho_0}\right]\Delta t\left[\xi^{1+n-m}\left[\psi^{\mathrm{iso}}+\psi^{\mathrm{ani}}\right]-\frac{1}{\rho_0^{*}}\rho_0\psi_0^{*}\right],\\
r_{\lambda^A} &= \lambda^A-\lambda_k^A-\left[1-q_{\lambda^A}\right]\Delta t\left[\left[\frac{\alpha}{2\beta}\exp\left(\beta[I_7-I_4]^2\right)+\frac{\mu}{2}I_7\right]^{-l}\right.\\
&\quad\left.\times\,\xi^{n}\rho_0\left[{}^{A}\psi^{\mathrm{nh}}+\psi^{\mathrm{ani}}\right]-{}^{\lambda^A}\psi_0^{*}\right],\\
\boldsymbol{r}_{\boldsymbol{n}^A} &= \boldsymbol{n}^A-\cos(\Delta t\omega)\boldsymbol{n}_k^A-[1-\cos(\Delta t\omega)]\\
&\quad\times\left[\boldsymbol{n}^{\omega}\cdot\boldsymbol{n}_k^A\right]\boldsymbol{n}^{\omega}-\sin(\Delta t\omega)\boldsymbol{n}^{\omega}\times\boldsymbol{n}_k^A.
\end{aligned} \tag{33}$$

While the corresponding linearisation for the two scalar-valued equations is straightforward, one must guarantee that $\boldsymbol{n}^A$ remains a unit vector. Practically speaking, one can either introduce an additional Lagrange term, which accounts for the normalisation constraint

$$\boldsymbol{r}_{\boldsymbol{n}^A}+\varsigma[\boldsymbol{n}^A\cdot\boldsymbol{n}^A-1]\mapsto\boldsymbol{r}_{\boldsymbol{n}^A}, \tag{34}$$

see Betsch and Steinmann 2002, or perform the linearisation with respect to the appropriate manifold (in terms of generalised coordinates often denoted as rotation parameters). In order to keep the formulation as concise and efficient as possible, we choose a parametrisation of the unit vector $\boldsymbol{n}^A$ in terms of spherical coordinates, say $\vartheta_{1,2}$ or $\theta_{1,2}$, that refer to a space-attached Cartesian frame $\{\boldsymbol{e}_{1,2,3}\}$, for example

$$\begin{aligned}
&\text{parametrisation 1}:\boldsymbol{n}^A\\
&\quad=\sin(\vartheta_1)\sin(\vartheta_2)\boldsymbol{e}_1+\cos(\vartheta_2)\boldsymbol{e}_2+\cos(\vartheta_1)\sin(\vartheta_2)\boldsymbol{e}_3,\\
&\text{parametrisation 2}:\boldsymbol{n}^A\\
&\quad=\cos(\theta_1)\sin(\theta_2)\boldsymbol{e}_1+\sin(\theta_1)\sin(\theta_2)\boldsymbol{e}_2+\cos(\theta_2)\boldsymbol{e}_3.
\end{aligned} \tag{35}$$

The first parametrisation is chosen throughout as long as $\mathrm{tol}<\vartheta_2<[\pi-\mathrm{tol}]$ with $0<\mathrm{tol}\ll 1$; the second parametrisation is applied otherwise (a third parametrisation is possible but not needed). For a general survey of the numerical treatment of finite rotations we refer the reader to Betsch et al (1998) and references cited therein.

With these relations at hand, the set-up of the (local monolithic) system of linear equations, which is solved for any iteration step, results in

$$\begin{bmatrix}
\partial_{\xi}r_{\xi} & \partial_{\lambda^A}r_{\xi} & \partial_{\vartheta_1}r_{\xi} & \partial_{\vartheta_2}r_{\xi}\\
\partial_{\xi}r_{\lambda^A} & \partial_{\lambda^A}r_{\lambda^A} & \partial_{\vartheta_1}r_{\lambda^A} & \partial_{\vartheta_2}r_{\lambda^A}\\
\partial_{\xi}r_{\vartheta_1} & \partial_{\lambda^A}r_{\vartheta_1} & \partial_{\vartheta_1}r_{\vartheta_1} & \partial_{\vartheta_2}r_{\vartheta_1}\\
\partial_{\xi}r_{\vartheta_2} & \partial_{\lambda^A}r_{\vartheta_2} & \partial_{\vartheta_1}r_{\vartheta_2} & \partial_{\vartheta_2}r_{\vartheta_2}
\end{bmatrix}\circ\begin{bmatrix}\Delta\xi\\ \Delta\lambda^A\\ \Delta\vartheta_1\\ \Delta\vartheta_2\end{bmatrix}=\begin{bmatrix}-r_{\xi}\\ -r_{\lambda^A}\\ -r_{\vartheta_1}\\ -r_{\vartheta_2}\end{bmatrix} \tag{36}$$

with (it is obvious that the residuals $r_{\vartheta_{1,2}}$ take different formats if parametrisation 2 in terms of $\theta_{1,2}$ is applied)

$$\begin{aligned}
&r_{\vartheta_2}=\vartheta_2-\bar{\vartheta}_2(\vartheta_{1,2},\ldots), && r_{\vartheta_1}=\vartheta_1-\bar{\vartheta}_1(\vartheta_{1,2},\ldots),\\
&\vartheta_2\doteq\arccos(n_2^A), && \vartheta_1\doteq\arccos(n_3^A)/\sin(\vartheta_2),\\
&\bar{\vartheta}_2\doteq\arccos(\bar{n}_2^A), && \bar{\vartheta}_1\doteq\arccos(\bar{n}_3^A)/\sin(\bar{\vartheta}_2),\\
&\boldsymbol{n}^A=\textstyle\sum_{i=1}^{3}n_i^A\boldsymbol{e}_i, && \bar{\boldsymbol{n}}^A\doteq\boldsymbol{n}^A-\boldsymbol{r}_{\boldsymbol{n}^A}=\textstyle\sum_{i=1}^{3}\bar{n}_i^A\boldsymbol{e}_i.
\end{aligned} \tag{37}$$

The (local) Jacobian itself is, however, not evaluated analytically, but rather approximated numerically by a first order perturbation scheme, for instance

$$\begin{aligned}
&\xi_{\varepsilon}=\xi+\varepsilon,\quad r_{\xi_{\varepsilon}}=r_{\xi}(\xi_{\varepsilon}\rho_0^{*},\boldsymbol{C},\boldsymbol{A};\boldsymbol{X}),\\
&\frac{1}{\varepsilon}[r_{\xi_{\varepsilon}}-r_{\xi}]\mapsto\partial_{\xi}r_{\xi},\qquad\ldots
\end{aligned} \tag{38}$$

with $\varepsilon\ll 1$. We do not give further details of the approach at this stage, but refer the reader to the contributions by Miehe (1996), Pérez-Foguet et al (2000a, b) and Fellin and Ostermann (2002) or Dennis and Schnabel (1996) for a general overview.

The same perturbation algorithm is adopted within a finite element context for the computation of the (global) algorithmic tangent; the exact evaluation for an isotropic setting being highlighted in, for example, Kuhl et al (2003). For convenience of the reader, we briefly summarise the numerical scheme and, following the outline in Miehe (1996), obtain the approximated algorithmic tangent operator as ($i,j,k,l=1,2,3$)

$$\begin{aligned}
&\boldsymbol{F}_{\varepsilon}=\boldsymbol{F}+\frac{\varepsilon}{2}[\bar{\boldsymbol{e}}_k\otimes[\bar{\boldsymbol{e}}_l\cdot\boldsymbol{F}]+\bar{\boldsymbol{e}}_l\otimes[\bar{\boldsymbol{e}}_k\cdot\boldsymbol{F}]],\\
&\boldsymbol{\sigma}_{\varepsilon}^{(kl)}=\boldsymbol{\sigma}^{(kl)}\left(\rho_0,\boldsymbol{F}_{\varepsilon}\cdot\boldsymbol{F}_{\varepsilon}^{\mathrm{t}},\boldsymbol{\alpha};\boldsymbol{X}\right),\\
&{}^{\mathrm{algo}}\mathfrak{e}_{\varepsilon}^{ij(kl)}=\frac{1}{\varepsilon}\left[\sigma_{\varepsilon}^{ij(kl)}-\sigma^{ij}\right]\\
&\quad-\frac{1}{2}[\delta^{ik}\sigma^{jl}+\delta^{il}\sigma^{jk}+\sigma^{ik}\delta^{jl}+\sigma^{il}\delta^{jk}],
\end{aligned} \tag{39}$$

where $\{\bar{\boldsymbol{e}}_{1,2,3}\}$ characterises an orthonormal frame, $\varepsilon\ll 1$; recall Eq. 24 for a representation of the Cauchy stress σ.

6 Numerical examples

For the subsequent numerical examples, a homogeneous deformation in uniaxial tension as well as 3-D finite element settings are considered. We therefore adopt the

formulation of enhanced eight node bricks (Q1E9) as advocated by Simo and Armero (1992) and do not place further emphasis on the finite element method itself; the reader is referred to the monographs by Oden (1972) or Belytschko et al (2000) and references cited therein.

The choice of appropriate material parameters is a non-trivial task and constitutes future research. In this (first) work we choose similar data to that applied in Holzapfel et al (2000) for the free Helmholtz energy density, namely $\lambda = 147$, $\mu = 3$ (which corresponds to $E = 8.94$, $\nu = 0.49$), $\alpha = 2$, $\beta = 1$ and $\rho_0|t_0 = \rho_0{}^* = 1$. The previously mentioned stability criterion is satisfied by, for instance, the exponents $n = 2$, $m = 4$ and in view of the fibre evolution we assume $l = 2.5$. The initial stimuli are chosen as ${}^{\rho_0}\psi_0^* = 2$ and ${}^{\lambda^A}\psi_0^* = 0.1$. Concerning the evolution or rather rotation of the fibre direction, $t^* = 100$ is assumed such that the relation $\Delta t \ll t^*$ holds for a typical time step size of $\Delta t = 1$. Finally, we mention that the perturbation parameter takes the value $\varepsilon = 10^{-8}$, where the selected machine precession accounts for 16 decimal points.

In order to visualise that two second order tensors do not commute, a scalar-valued field called the "anisotropy measure" is introduced, which takes the following format

$$\delta(\boldsymbol{C}\cdot\boldsymbol{S}) = \frac{||[\boldsymbol{C}\cdot\boldsymbol{S}] - [\boldsymbol{C}\cdot\boldsymbol{S}]^{\mathrm{t}}||}{||\boldsymbol{C}\cdot\boldsymbol{S}||}. \tag{40}$$

6.1 Uniaxial tension

To set the stage we first discuss a homogeneous deformation in uniaxial tension, in other words $\boldsymbol{F} \doteq \boldsymbol{I} + [\lambda_3{}^U - 1]\boldsymbol{e}_1 \otimes \boldsymbol{e}_1$. The scalar $\lambda_3{}^U$ obviously denotes the longitudinal stretch and the chosen loading path is determined by $\lambda_3{}^U = 1.15$ for $t \in (0,25]$ and $\lambda_3{}^U = 1.30$ for $t \in (25,50]$. The initial fibre (direction) takes the representation $\boldsymbol{a}|_{t_0} = 0.866\boldsymbol{e}_1 + 0.5\boldsymbol{e}_2$ such that the initial angle between $\boldsymbol{a}|_{t_0}$ and the Cartesian axis $\boldsymbol{e}_1$, say $\phi_{\boldsymbol{a}} = \angle(\boldsymbol{a},\boldsymbol{e}_1)$, corresponds to $\phi_{\boldsymbol{a}}|_{t_0} = \pi/6$. In analogy to $\phi_{\boldsymbol{a}}$, we also monitor the angles $\phi_{\boldsymbol{C}} = \angle(\boldsymbol{n}_3{}^C, \boldsymbol{e}_1)$ and $\phi_{\boldsymbol{S}} = \angle(\boldsymbol{n}_3{}^S, \boldsymbol{e}_1)$ in the following. Moreover, $\sigma^{11} = \boldsymbol{e}_1 \cdot \boldsymbol{\sigma} \cdot \boldsymbol{e}_1$ denotes the component of the Cauchy stress in the longitudinal direction, see remark 3. In order to get a more pronounced view of the behaviour of the developed framework, we first focus on the separate evolution of ρ_0, λ^A and $\boldsymbol{n}^A$ and second, address combinations thereof (conveniently realised via the parameters $q_{\rho_0,\ \lambda^A,\ \boldsymbol{n}^A}$).

6.1.1 *Referential density evolution*

Placing emphasis solely on the evolution of the referential density, in other words $q_{\rho_0} = 0$ and $q_{\lambda^A} = q_{\boldsymbol{n}^A} = 1$, we observe an initial decrease, and later on, an increase in the (referential) relative density field ξ under the applied load levels, see Fig. 1. The driving term ${}^{\rho_0}\psi_0$

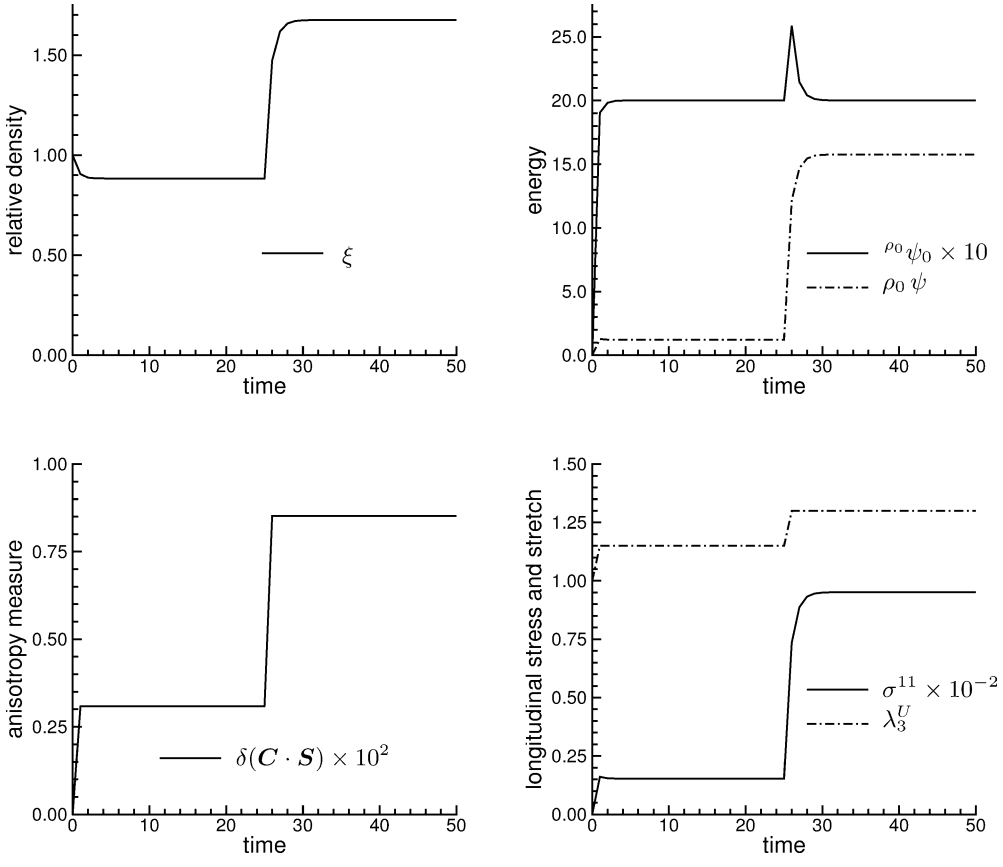

Fig. 1 Uniaxial tension: density evolution ($q_{\rho_0} = 0$, $q_{\lambda^A} = q_{\boldsymbol{n}^A} = 1$)

(recall Eq. 27) adapts to the stimulus ${}^{\rho_0}\psi_0^*$ and the free Helmholtz energy converges towards a plateau. Both the anisotropy measure $\delta(\boldsymbol{C}\cdot\boldsymbol{S})$ as well as the stress component σ^{11} clearly monitor the block-type loading path.

6.1.2 Fibre strength evolution

Now, with the fibre strength being the only additional field that underlies an evolution, $q_{\lambda^A}=0$ and $q_{\rho_0}=q_{\boldsymbol{n}^A}=1$, we obtain a qualitatively similar response for λ^A as for ξ in the previous setting (even though the final fibre strength is constantly below its initial value), compare Fig. 2. The adjustment of the driving term ${}^{\lambda^A}\psi_0$ (recall Eq. 29) with the stimulus ${}^{\lambda^A}\psi_0^*$, in other words the cessation of the evolution of λ^A, is clearly visualised. Once more, the free Helmholtz energy shows a plateau-type response. It is obvious for the considered model-type that the anisotropy measure $\delta(\boldsymbol{C}\cdot\boldsymbol{S})$ is directly related to the processing of λ^A. The stress component σ^{11} is however still aligned with the block-type loading path.

6.1.3 Fibre direction evolution

We first highlight the evolution of the fibre direction $\boldsymbol{n}^A$ aligned with the principal strain direction $\boldsymbol{n}_3{}^C$; with $q_{\boldsymbol{n}^A}=0$ and $q_{\rho_0}=q_{\lambda^A}=1$. Since $\boldsymbol{n}_3{}^C=\boldsymbol{e}_1$ holds throughout for the considered type of deformation ($\phi_{\boldsymbol{C}}=0$), we consequently observe that $\phi_{\boldsymbol{a}}$ is monotonically decreasing while $\phi_{\boldsymbol{S}}$ increases, see Fig. 3. The graph of the free Helmholtz energy again shows a plateau-type response, whereby convergence from the bottom is observed. This effect is due to the fact that the fibre rotates until $\phi_{\boldsymbol{a}}=0$ and so stiffens the material. Consequently, the free Helmholtz energy increases during this process. In analogy to $\phi_{\boldsymbol{a}}$, the anisotropy measure $\delta(\boldsymbol{A}\cdot\boldsymbol{A}|_{t_0})$, which underlines the non-commutativity of the actual and initial (referential) structural tensor, is monotonically increasing, while $\delta(\boldsymbol{C}\cdot\boldsymbol{S})$ reflects the combination of block-type stress response (σ^{11}) and the adaptation of $\boldsymbol{n}^A$ with $\boldsymbol{n}_3{}^C=\boldsymbol{e}_1(\phi_{\boldsymbol{a}}\searrow 0$ for $t\nearrow\infty)$.

Second, let the evolution of the fibre direction $\boldsymbol{n}^A$ be aligned with the principal stress direction $\boldsymbol{n}_3{}^S$; with $q_{\boldsymbol{n}^A}=0$ and $q_{\rho_0}=q_{\lambda^A}=1$. We consequently obtain a monotonically increasing response of $\phi_{\boldsymbol{a}}$ as $\phi_{\boldsymbol{S}}\nearrow\pi/2$ for $t\nearrow\infty$, see Fig. 4. Plotting the free Helmholtz energy, one observes a plateau-type result with convergence from the top. The rotation of the fibre apparently softens the material since the principal strain directions are fixed and the angle between $\boldsymbol{n}^A$ and $\boldsymbol{n}_3{}^C$ is monotonically increasing. The anisotropy measure $\delta(\boldsymbol{A}\cdot\boldsymbol{A}|_{t_0})$ demonstrates the evolution of the structural tensor and $\delta(\boldsymbol{C}\cdot\boldsymbol{S})$ nevertheless highlights the tendency towards the coaxiality of stress and strain.

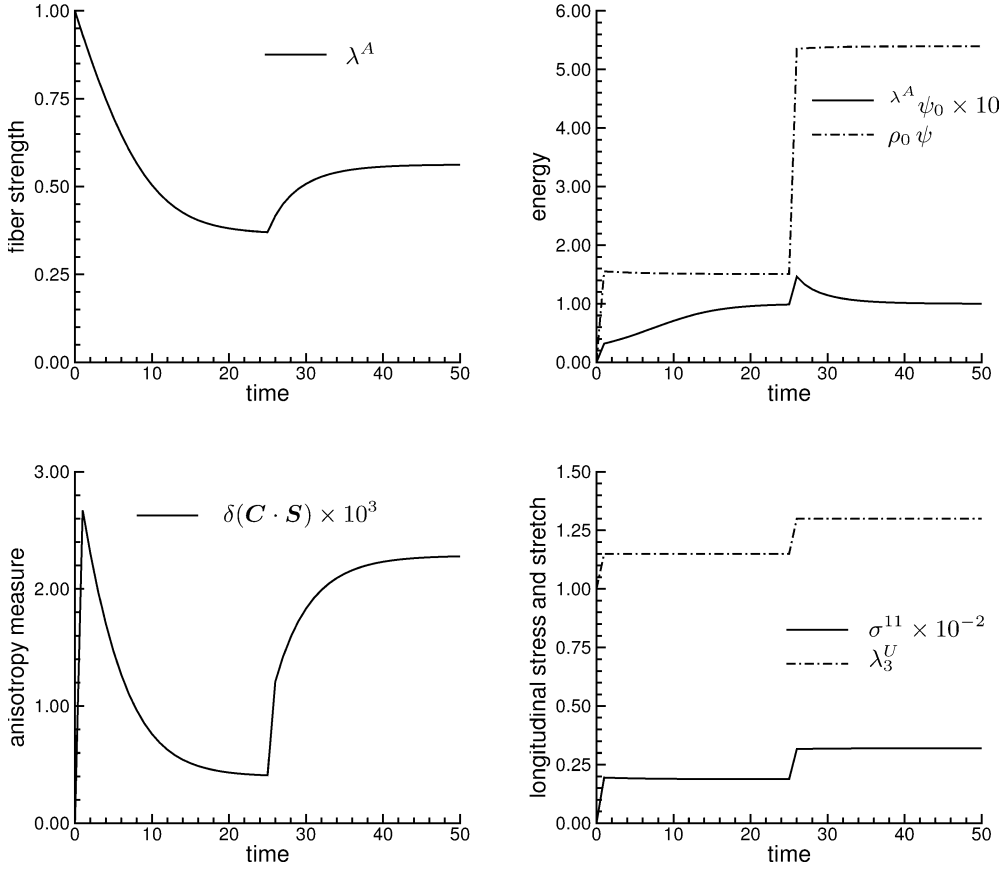

Fig. 2 Uniaxial tension: fibre strength evolution ($q_{\lambda^A}=0$, $q_{\rho_0}=q_{\boldsymbol{n}^A}=1$)

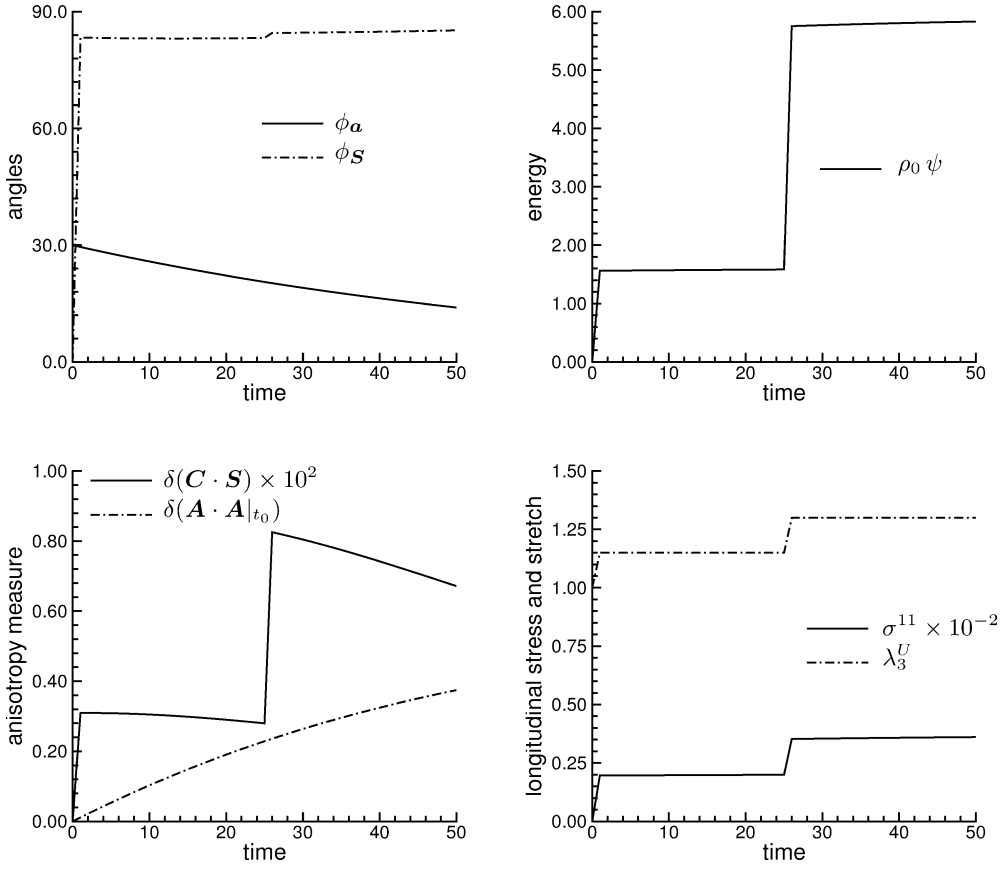

Fig. 3 Uniaxial tension: fibre direction evolution, aligned with $\boldsymbol{n}_3^C$ ($q_{\boldsymbol{n}^A}=0$, $q_{\rho_0}=q_{\lambda^A}=1$)

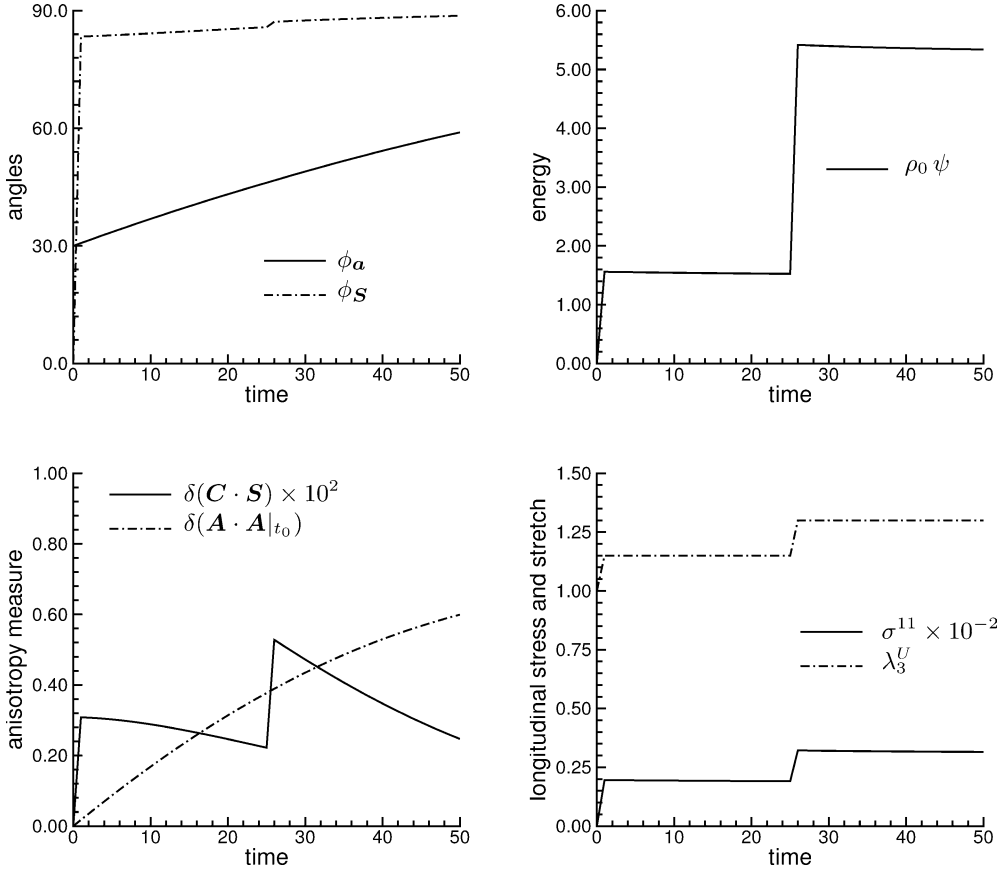

Fig. 4 Uniaxial tension: fibre direction evolution, aligned with $\boldsymbol{n}_3^S$ ($q_{\boldsymbol{n}^A}=0$, $q_{\rho_0}=q_{\lambda^A}=1$)

6.1.4 *Evolution of the referential density, the fibre strength and direction*

In order to complete the discussion of the homogeneous deformation in uniaxial tension, let all three arguments, ρ_0 or ξ, λ^A and $\boldsymbol{n}^A$ develop during the deformation process; with $q_{\boldsymbol{n}^A} = q_{\rho_0} = q_{\lambda^A} = 0$. Fig. 5 monitors the results for $\boldsymbol{n}^A$ following ${\boldsymbol{n}_3}^C$ in analogy to the previous figures. We observe in particular that ξ and λ^A first decrease and then increase. The driving terms for their evolution align with the corresponding stimuli and the free Helmholtz energy results once again in a plateau-type graph. Monotonically decreasing properties characterise the evolution of $\phi_{\boldsymbol{a}}$ and the anisotropy measures as well as the longitudinal stress level result in similar diagrams as for the previous examples.

Finally, let $\boldsymbol{n}^A$ evolve with ${\boldsymbol{n}_3}^S$; with $q_{\boldsymbol{n}^A} = q_{\rho_0} = q_{\lambda^A} = 0$. Fig. 6 presents the results obtained in analogy to Fig. 5. Placing emphasis on only two properties of this computation, we point out the fact that the free Helmholtz energy, as well as the longitudinal stress (σ^{11}), address smaller values as for the previous setting, compare Fig. 5, which agrees with the conclusions in Sect. 6.1.3.

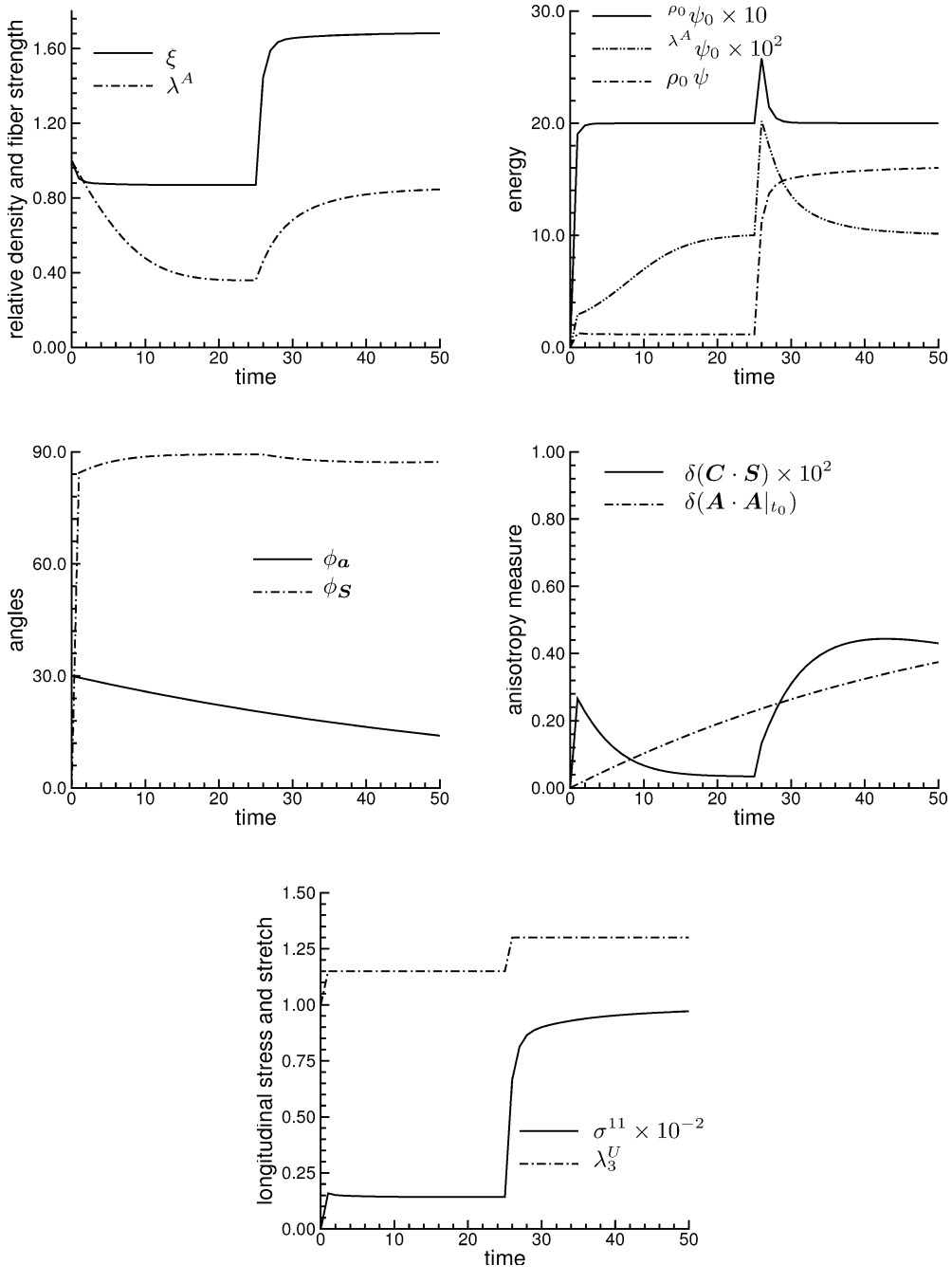

Fig. 5 Uniaxial tension: evolution of the density, the fibre strength and direction, aligned with ${\boldsymbol{n}_3}^C$ ($q_{\boldsymbol{n}^A} = q_{\rho_0} = q_{\lambda^A} = 0$)

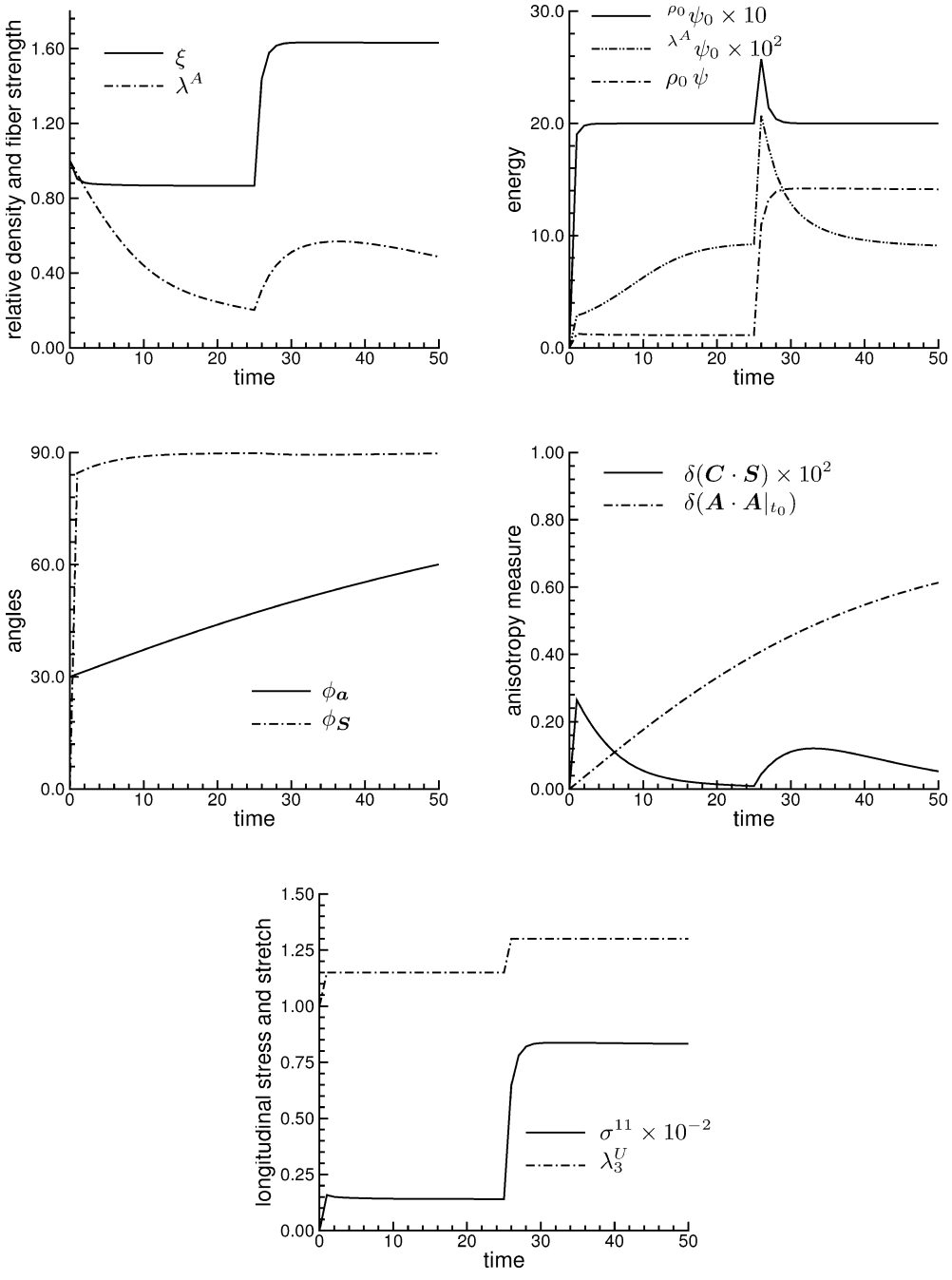

Fig. 6 Uniaxial tension: evolution of the density, the fibre strength and direction, aligned with $\boldsymbol{n}_3^S$ ($q_{\boldsymbol{n}^A} = q_{\rho_0} = q_{\lambda^A} = 0$)

6.2 Specimen under tension

In analogy to the previous examples in Sect. 6.1, where a homogeneous deformation in uniaxial tension has been documented in detail, we now focus on a 3-D finite element setting. For comparison reasons, we first discuss a specimen under tension ($\boldsymbol{e}_1$ once more corresponds to the loading direction). Some material parameters, however, are slightly modified; $\lambda = 32$, $\mu = 3.3$ (such that $E = 8.94$ and $\nu = 0.4$), $m = 3$, $l = 1.1$, $t^* = 0.5 > \Delta t = 0.05$, ${}^{\rho_0}\psi_0^* = 1$ and $\boldsymbol{a}|_{t_0} = 0.5\ \boldsymbol{e}_1 + 0.866\ \boldsymbol{e}_2$. All remodelling fields therefore evolve throughout, namely the density as well as the fibre strength and direction, which is aligned with the strain field ($q_{\rho_0} = q_{\lambda^A} = q_{\boldsymbol{n}^A} = 0$). The discretisation of the considered specimen with dimensions 1×1×0.1 is performed by 10×10×2 eight node bricks, see Fig. 7, where the boundary and loading conditions are highlighted. In particular, note that the loading direction and the initial fibre direction are not coaxial, such that the stress state is highly inhomogeneous from the outset. In fact, we incrementally increase a longitudinal force (F_1, as represented by a constant loading tensile stress with respect to the reference configuration) within five time steps and then fix this force for another 45 time steps. Moreover, due to the chosen fibre direction, one observes that the maximal longitudinal displacements

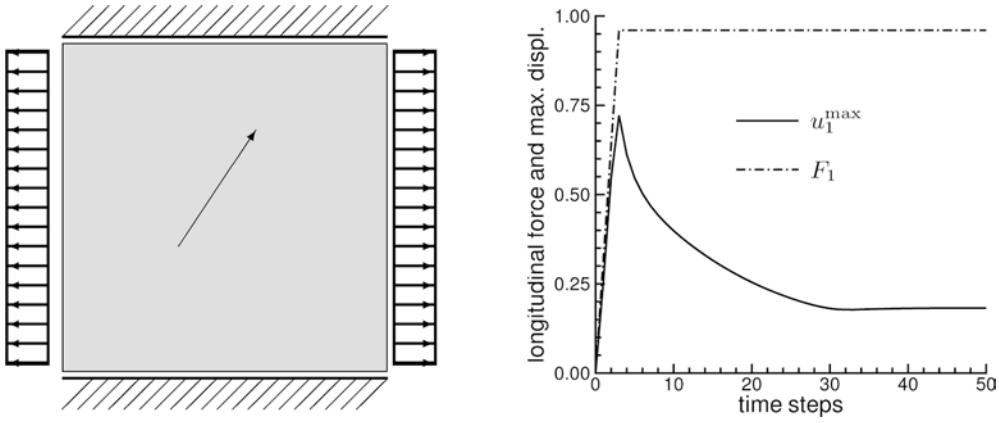

Fig. 7 Specimen under tension: geometry and boundary conditions (*left*), maximal longitudinal displacement $u_1{}^{\max}$ and loading history F_1 (*right*)

($u_1{}^{\max}$) occur constantly at the bottom right and top left corner of the body, respectively, see the plots in Fig. 7. Since the remodelling process (here) stiffens the material, the displacements increase at first and then decrease, which is clearly shown in Fig. 8 where the deformed mesh is highlighted at different time steps. Completing this example, Figs. 9 and 10 highlight the contribution of the density, the fibre strength, the anisotropy measure and the reorientation of the fibre (with respect to the initial, undeformed, mesh) at different time steps. The temporal evolution of these fields is therefore clearly apparent, especially the alignment of the fibres according to the loading direction.

6.3 Specimen under shear

Similar to the above specimen under tension-type loading, we now discuss a 3-D finite element setting under shear. Identical dimensions (1×1×0.1) are adopted, the same discretisation (10×10×2 eight node bricks, Q1E9) is chosen and the material parameters likewise coincide with those given in Sect. 6.2, except for $t^* = 5 \gg \Delta t = 0.05$. Moreover, the initial fibre direction has been aligned with the moving direction of the upper edge; in other words $\boldsymbol{a}|_{t_0} = \boldsymbol{e}_1$, see Fig. 11 where the boundary and loading conditions are documented (note in particular that the bottom edge is clamped). The overall deformation process is therefore highly inhomogeneous right from the start. Once more, all remodelling fields are active ($q_{\rho_0} = q_{\lambda^A} = q_{\boldsymbol{n}^A} = 0$) and the fibre direction aligns with the predominant principal strain direction. Practically speaking, the top edge is constrained such that all relevant finite element nodes are subjected to the same displacement field. The resultant force in the horizontal direction of these nodes (F_1) is incrementally increased within five time steps and then held constant for another 45 time steps. As a result, we observe that the maximal horizontal displacements ($u_1{}^{\max}$), which are located constantly at the top edge, first increase during the first five time steps and then decrease. This effect stems from the stiffening of the remodelling process; see Figs. 11 and 12 where the deformed mesh is represented at different time steps. In analogy to the previous example, the contributions of the density, the fibre strength, the anisotropy measure, and the reorientation of the fibre are visualised at different time steps, see Fig. 13 and 14. The results clearly show that the specimen tends to stiffen (both ρ_0 and λ^A) along the diagonal in the x-y plane. The anisotropy measure $\delta(\boldsymbol{C}\cdot\boldsymbol{S})$ apparently also takes its peak values in the same domain and, moreover, the visualisation of the fibre direction underlines the alignment with respect to the predominant principal strain direction.

6.4 Specimen with surface cut

Finally, we discuss a specimen with a surface cut, which is again subject to tension-type loading. The denomination of this example as a "cut" might be somehow misleading, since many additional responses are involved when biological tissues are disrupted. For conceptual simplicity, however, we refer to this setting as a cut, even though the overall behaviour rather reflects the effect of wound healing.

The dimensions of the specimen are chosen as 2×1×0.5, and the discretisation is performed with 16×8×4 eight node bricks (Q1E9); see Figs. 15 and 16. To be specific, the force-driven loading conditions correspond to initially uniform axial stresses at the top and bottom sides. For notational simplicity, let this longitudinal loading direction be aligned with the Cartesian axis $\boldsymbol{e}_1$ (such that the initial configuration of the body lies in the domain $\{-1 \le X_1 \le 1, -\frac{1}{2} \le X_2 \le \frac{1}{2}, 0 \le X_3 \le \frac{1}{2}\}$). The initial (closed) surface cut is however perpendicular to the loading direction, collinear with $\boldsymbol{e}_2(\phi_{\text{cut}}|_{t_0} = \angle(\text{cut}, \boldsymbol{e}_2)|_{t_0} = 0)$, and its dimensions are correlated with half of the width and thickness of the specimen, respectively. Even though the underlying material is anisotropic, it is sufficient to constrain the degrees of freedom of just a few nodes. In particular, the displacements of just three nodes, namely the mid-nodes under the bottom of the cut, are controlled; in other words $u^{\text{pr}}_{1,2,3}|_{\boldsymbol{X}=14\boldsymbol{e}_3} = 0$ and $u^{\text{pr}}_{1,2}|_{\boldsymbol{X}=18\boldsymbol{e}_3,\boldsymbol{0}} = 0$. Moreover, the material parameters incorporated are identical to the set formerly applied in Sect. 6.3 with ${}^{\rho_0}\psi_0^* =$

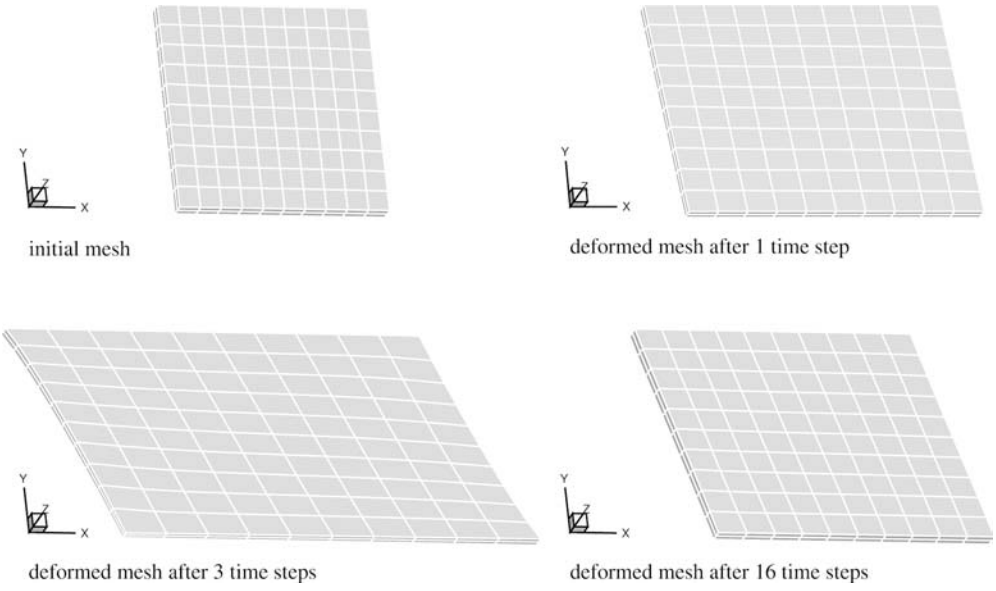

Fig. 8 Specimen under tension: initial mesh and deformed meshes after 1-, 3- and 16 time steps

0.5 and ${}^{\lambda^A}\psi_0^* = 0.05$ being the only exceptions. The initial fibre direction is chosen as $\boldsymbol{a}|_{t_0} = 0.866\boldsymbol{e}_1 + 0.5\boldsymbol{e}_2$ and, in analogy to the previous settings, all remodelling fields are active ($q_{\rho_0} = q_{\lambda^A} = q_{\boldsymbol{n}^A} = 0$).

Besides the chosen boundary conditions, Fig. 15 additionally highlights the entire load versus displacement curve in terms of the longitudinal force (F_1) and the maximal longitudinal displacement, which refers constantly to the top left ($-u_1{}^{\max}$) and bottom right nodes ($u_1{}^{\max}$). It is clearly apparent that the chosen loading path corresponds to a linear increase in the resultant longitudinal force within a period of ten time steps while this force is held constant for the subsequent 40 time steps. In analogy to the numerical examples discussed above, we observe that the maximal longitudinal displacement first increases with increasing load, but, due to the remodelling of the material, decreases in the progression. This stiffening effect is shown in Fig. 16, where deformed meshes for different time steps are highlighted. Similar to the numerical examples in Sects. 6.2 and 6.3, Figs. 17 and 18 visualise the contributions of the density, the fibre diameter, the anisotropy measure, and the fibre direction for different time steps. As expected, one observes on the one hand that the material stiffens at the tips of the cut, where ρ_0 and λ^A take their peak values. On the other hand, it is apparent that the material softens in the areas on the left and right sides of the edges of the cut. From a medical point of view, this cut orientation is therefore often disadvantageous since the cut is not collinear with the dominant principal stress (or strain) direction; in other words it is not collinear with respect to the corresponding (Langer's) cleavage lines. Finally, the graphical representation of the anisotropy measure and the fibre direction itself in Fig. 18 underlines that the stress field, or the fibre respectively, aligns with the strain field (in time).

The influence of a deviation in the orientation of the cut is displayed in Fig. 19. Even though the overall response, namely the longitudinal force versus maximal longitudinal displacement curve, turns out to be almost independent of the chosen orientation of the cut (here $\phi_{\text{cut}}|_{t_0} \in \{-\pi/6,\ 0,\ \pi/6\}$), we obtain different density and fibre contributions.

7 Discussion

7.1 Summary

This work aimed at the development of a theoretical and computational framework that describes the remodelling of biological tissues. Typical examples of such adaptation processes are growth phenomena and rearrangements of internal microstructures. In this context, isotropic growth has been addressed via a Wolff-type evolution law for the referential density, where the additional mass flux term has been neglected for conceptual simplicity. We introduced the underlying microstructure of the tissue via the well-established ansatz of the incorporation of a fibre direction. This framework apparently resulted in an anisotropic response function for the linear momentum flux; to be specific, the material is modelled as transversely isotropic. The direction and the strength or diameter of the fibre were not constrained to remain constant during the deformation of the considered body. We adopted a Wolff-type law for the fibre strength as well, in analogy to the density field, which accordingly possessed similar saturation-type characteristics as the density evolution. It is then the combination of both contributions which is consequently classified as isotropic and anisotropic growth or simply as anisotropic growth. Moreover, the reorientation of the fibre is in general of cardinal importance. Following the idea that the stored energy, with respect to an anisotropic material body, takes an extremum if the principal axes of stress and strain

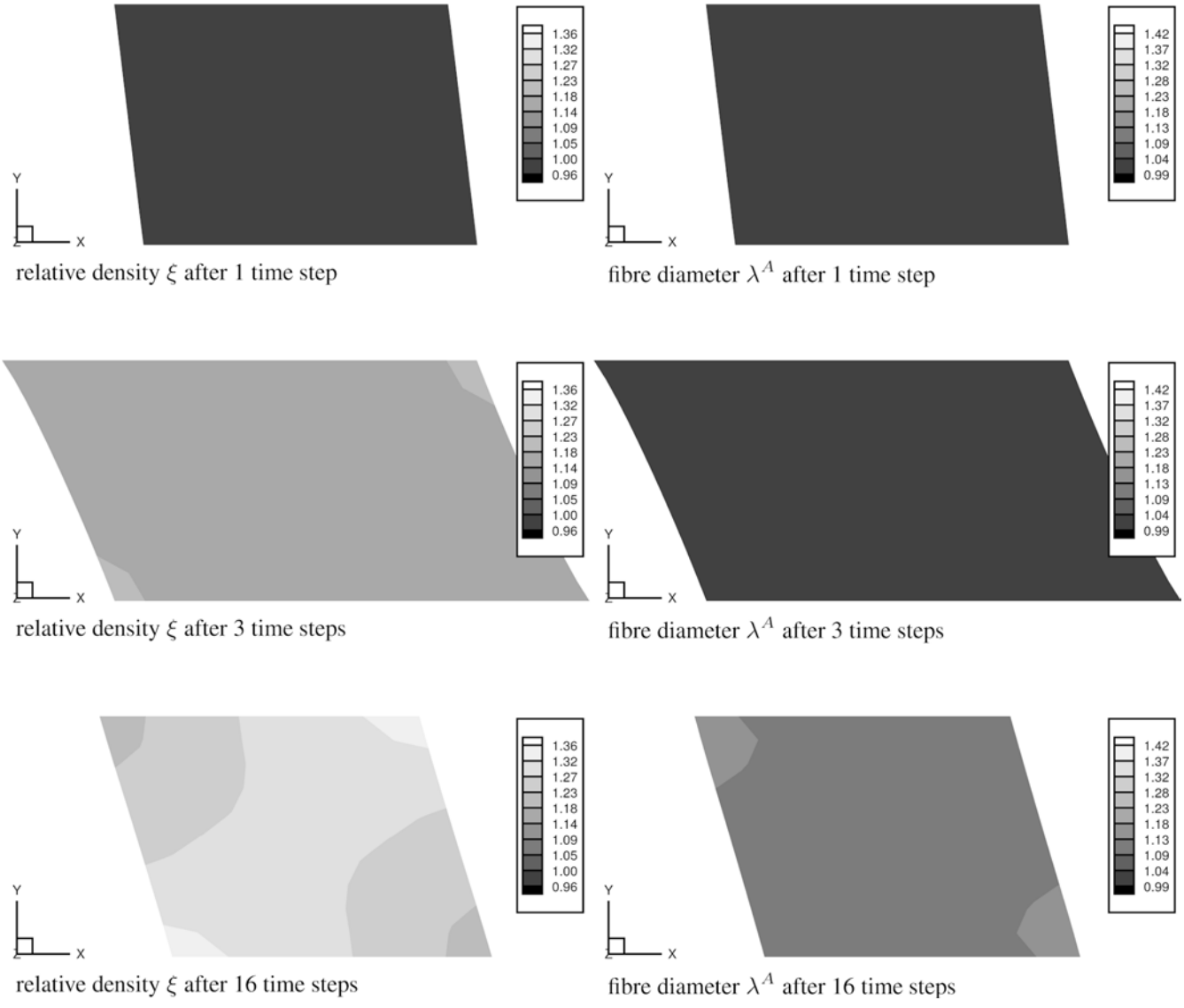

Fig. 9 Specimen under tension: relative density ξ (*left*) and fibre diameter λ^A (*right*) after 1, 3, and 16 time steps

coincide, we set up a relaxation-type evolution equation for the rotation of the fibre.

7.2 Conclusions

The advantage of the proposed formulation is the opportunity to separately address the anisotropic growth, or rather the strengthening and the reorientation of the fibre. Furthermore, issues of implementation are developed, such that the theoretical framework is especially suited for numerical applications, like those based on the finite element method. As an interesting side aspect, the proposed formulation fits nicely into common finite element codes since the standard framework of internal variables has been adopted.

There are nevertheless still several (known) factors left that apparently influence the remodelling process but are not addressed here, including electric stimuli, age dependency, damage effects after peak loads or particular healing mechanisms, even though a number of remodelling effects are captured by the proposed framework. The applied format of the Wolff-type evolution laws seems to be quite powerful in the present context. Their particular representation, however, could be extended in order to include so-called dead zones and different response characteristics for increase and decrease; in other words growth and shrinkage. Other types of evolution laws should be compared with the Wolff-type ansatz adopted in this work. The proposed type of evolution equations, as well as the concept of an energy extremum, are widely accepted for the modelling of hard tissues. The simulation of soft tissues, however, could also be based on more general concepts. Any evaluation and validation of different models should of course rest upon biological reasoning and experimental data.

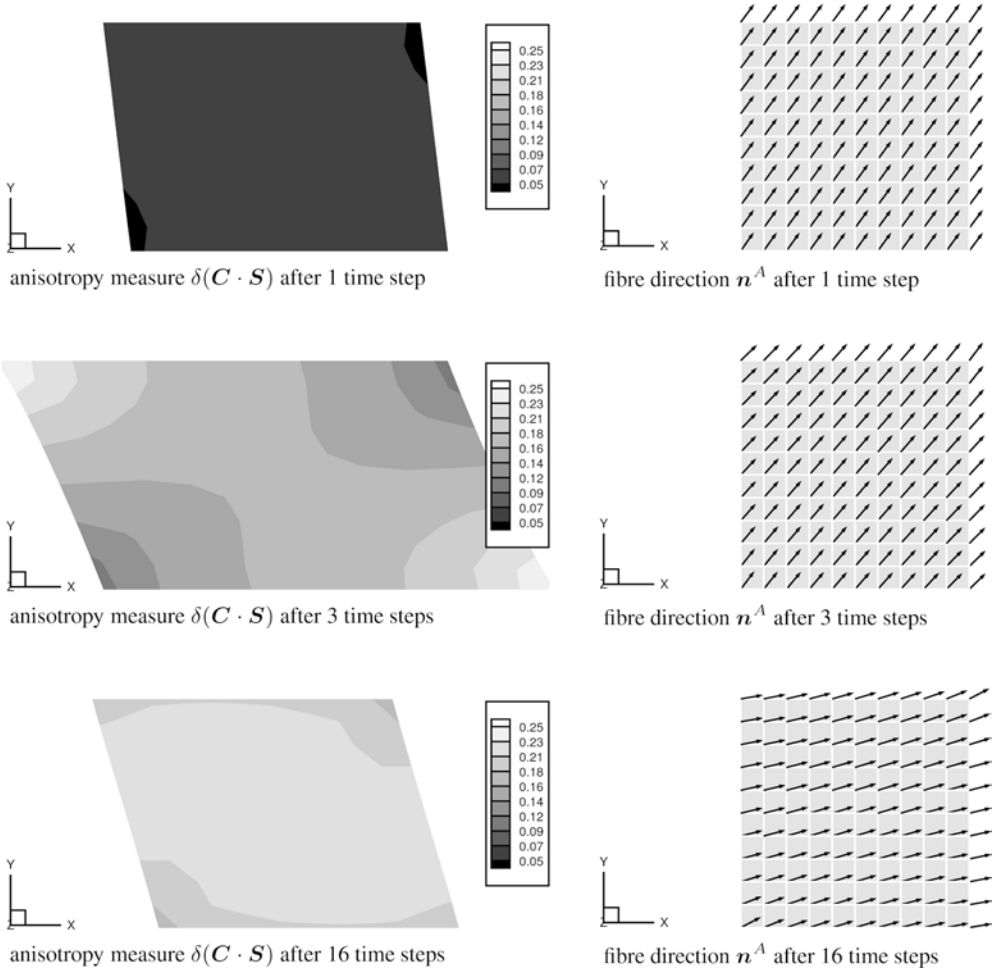

Fig. 10 Specimen under tension: anisotropy measure $\delta(\boldsymbol{C}\cdot\boldsymbol{S})$ (*left*) and fibre direction $\boldsymbol{n}^A$ (*right*) after 1, 3, and 16 time steps

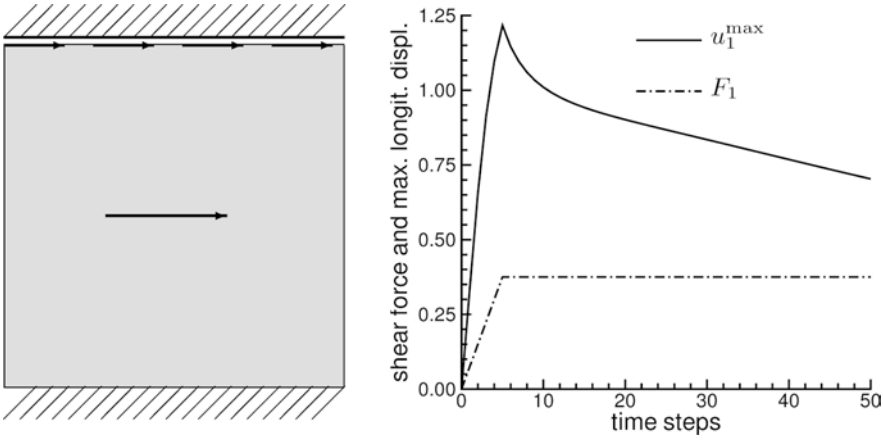

Fig. 11 Specimen under shear: geometry and boundary conditions (*left*), maximal horizontal displacement $u_1{}^{\max}$ and loading history F_1 (*right*)

7.3 Outlook

7.3.1 Incorporation of residual stresses

As previously mentioned in remark 1, a minor modification of the (anisotropic part of the) weighted free Helmholtz energy density enables us to capture a particular format of residual stress, $\boldsymbol{S}^{\text{res}}$ (such that $\boldsymbol{S}|_{\boldsymbol{C}=\boldsymbol{I}} = \boldsymbol{S}^{\text{res}}|_{\boldsymbol{C}=\boldsymbol{I}}$) or $\boldsymbol{\sigma}^{\text{res}}$ ($\boldsymbol{\sigma}|_{\boldsymbol{b}=\boldsymbol{i}} = \boldsymbol{\sigma}^{\text{res}}|_{\boldsymbol{b}=\boldsymbol{i}}$), respectively; recall that an equilibrated body with vanishing surface traction and vanishing body forces might exhibit residual stress, while initial stresses might occur in equilibrated bodies with non-zero surface traction and non-zero body forces. A classical and enlightening survey on this topic is given by Biot (1965). The reader is also referred to the contributions on initial stress by Green et al (1952), Truesdell (1966), Truesdell and Noll (2004), Iesan (1989), Ciarletta and Iesan (1993) or Haupt et al (1992) as well as the

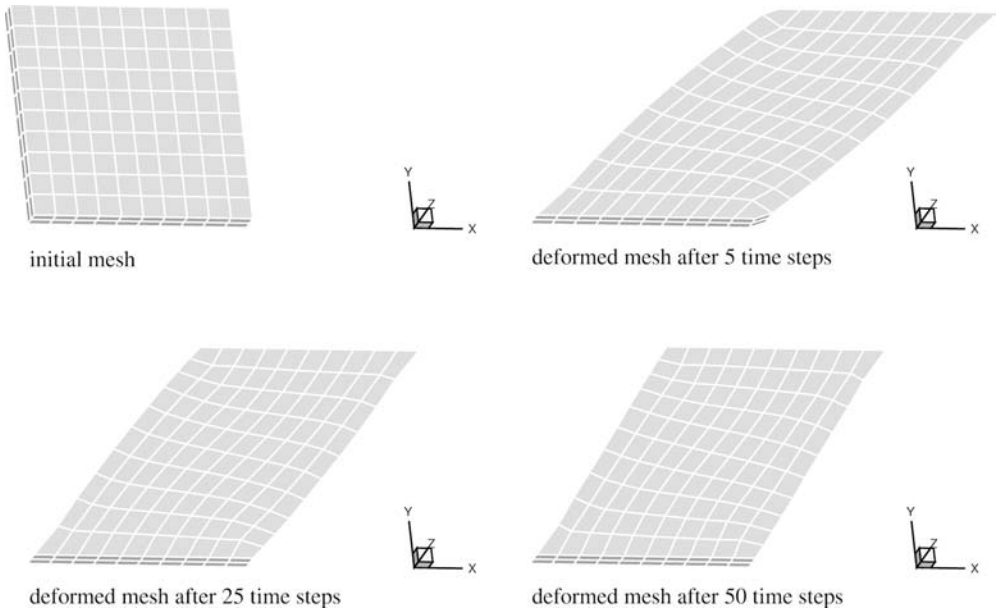

Fig. 12 Specimen under shear: initial mesh and deformed meshes after 5, 25, and 50 time steps

elaborations on internal constraints in Antman (1995) or Podio-Guidugli (2000). The pioneering work on residual stresses by Hoger is documented in a series of papers (mainly in the Journal of Elasticity), for instance Hoger (1993a, b, c, 1996, 1997); see also the contribution by Skalar et al (1996). The main idea within a finite strain framework consequently relies on the incorporation of the (symmetric) residual stress field as an additional argument into the free Helmholtz energy density; see, for instance, the contributions in Boehler (1987) or Antman (1995) for an overview of the underlying representation theorems. Apparently, the overall material response then turns out to be anisotropic since the residual stress is generally not aligned with the subsequent loading path; in this context, note that, for elastoplastic behaviour, effects like (anisotropic) kinematic hardening as represented by a modified yield function allow similar interpretations to the incorporation of a residual stress into the free Helmholtz energy density.

Recalling the particular prototype model as developed in Sect. 4, one consequently obtains from $\psi^{\text{ani}} = \psi^{\text{ani}}(\rho_0, I_7, I_4; \boldsymbol{X})$ and $\boldsymbol{S}^{\text{ani}} = 2\rho_0 \partial_{\boldsymbol{C}} \psi^{\text{ani}}$, the (rank one) stress contribution

$$\boldsymbol{S}^{\text{ani}} = 2\rho_0 \partial_{\boldsymbol{C}} \psi^{\text{ani}} = S_7 \boldsymbol{A}, \quad \boldsymbol{\sigma}^{\text{ani}} = J^{-1} S_7 \boldsymbol{\alpha}$$
$$\text{with } S_7 = 2\alpha \left[\frac{\rho_0}{\rho_0^*}\right]^n [I_7 - I_4] \exp(\beta [I_7 - I_4]^2). \tag{41}$$

A slight modification of ψ^{ani} enables us to motivate a residual stress relation, which is solely driven by the fibre evolution. To be specific, the variation $\psi^{\text{ani}}(\rho_0, I_7, i_4; \boldsymbol{X})$ suggests the relation $\psi^{\text{res}}(\rho_0, I_4, i_4; \boldsymbol{X})$ such that, for example, $\boldsymbol{S}^{\text{res}} \doteq 2\partial_{\boldsymbol{C}} \psi^{\text{res}}$ with $i_4 \doteq \text{const}$. To be specific, we end up with the following format for the reactive or residual stress (which is deformation-induced here, but please note that unloading might take place on a different, for instance, smaller timescale)

$$\begin{aligned}
\boldsymbol{S}^{\text{res}} &= S_{\text{res}} \boldsymbol{A} \quad \text{with} \quad S_{\text{res}} \\
&= 2\alpha \left[\frac{\rho_0}{\rho_0^*}\right]^n [I_4 - i_4] \exp\left(\beta [I_4 - i_4]^2\right), \\
\boldsymbol{\sigma}^{\text{res}} &= \sigma_{\text{res}} \boldsymbol{\alpha} \quad \text{with} \quad \sigma_{\text{res}} = J^{-1} S_{\text{res}} \quad \text{and} \\
\nabla_{\boldsymbol{x}} \cdot \boldsymbol{\sigma}^{\text{res}} &= [[\nabla_{\boldsymbol{x}} \otimes [\sigma_{\text{res}} \lambda^\alpha] + \sigma_{\text{res}} \lambda^\alpha \nabla_{\boldsymbol{x}}] \cdot \boldsymbol{n}^\alpha] \boldsymbol{i} \\
&\quad + \sigma_{\text{res}} \lambda^\alpha \nabla_{\boldsymbol{x}} \otimes \boldsymbol{n}^\alpha] \cdot \boldsymbol{n}^\alpha \doteq 0 \quad \text{in} \quad \mathscr{B}_t, \\
\boldsymbol{\sigma}^{\text{res}} \cdot \boldsymbol{n} &= \sigma_{\text{res}} \lambda^\alpha [\boldsymbol{n}^\alpha \cdot \boldsymbol{n}] \boldsymbol{n}^\alpha \doteq \boldsymbol{0} \quad \text{on} \quad \partial\mathscr{B}_t,
\end{aligned} \tag{42}$$

which stems from $[I_7 - i_4] \neq 0$ for $\boldsymbol{C} = \boldsymbol{I}$; here $\boldsymbol{n}$ denotes the outward surface normal (with $\boldsymbol{n} \cdot \boldsymbol{n} = 1$), the spatial second order identity is introduced via $\boldsymbol{i}$, additional body or volume forces are neglected, and the reader is referred to remark 3 for further notational details. Transverse isotropy actually turns out to be the simplest symmetry group that supports residual stresses. From Eq. 42 we immediately observe that $\boldsymbol{S}^{\text{res}}$ and σ^{res} respectively (symmetric, rank one, no spherical contributions) preserve the underlying material symmetry group. Please note that this representation is obtained by a constitutive law and that the evolution equation for the fibre diameter and direction should be adjusted for the problem at hand. Moreover, residual stresses subject to some body of interest are always inhomogeneous due to the constraints highlighted in Eq. 42, which result (with the residual stress being symmetric) in

$$\begin{aligned}
\int_{\mathscr{B}_t} \boldsymbol{\sigma}^{\text{res}} \, \mathrm{d}v &= \int_{\partial\mathscr{B}_t} [\boldsymbol{\sigma}^{\text{res}} \cdot \boldsymbol{n}] \otimes \boldsymbol{x} \, \mathrm{d}a \\
&\quad - \int_{\mathscr{B}_t} [\nabla_{\boldsymbol{x}} \cdot \boldsymbol{\sigma}^{\text{res}}] \otimes \boldsymbol{x} \, \mathrm{d}v = \boldsymbol{0},
\end{aligned} \tag{43}$$

see for instance Ogden 1997 or Chadwick 1999. Furthermore, the initial residual stress vanishes for the particular ansatz $i_4 = ||\boldsymbol{A}||_{t_0}$. For physical reasons

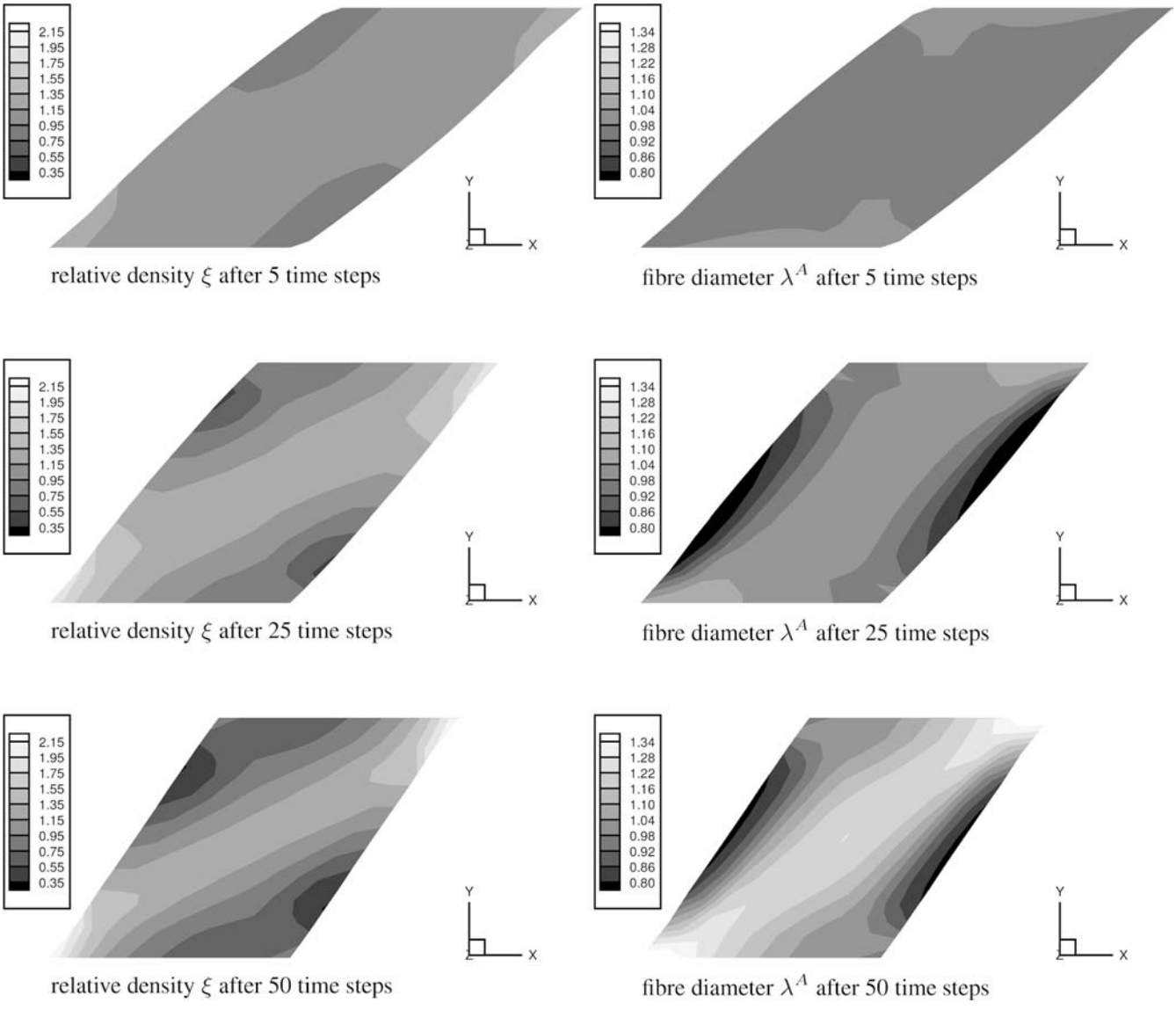

Fig. 13 Specimen under shear: relative density ξ (*left*) and fibre diameter λ^A (*right*) after 5, 25, and 50 time steps

however, the choice $i_4 \geq ||\boldsymbol{A}||_{t_0}$ seems to be appropriate since the strengthening of fibres then causes residual stresses, which are related to tension and not to compression.

7.3.2 Extension to orthotropic symmetry

It turned out that the formulation of reorienting fibres is still manageable and that the corresponding implementation is somewhat straightforward. The next step consists of the extension of the transversely isotropic behaviour to an orthotropic material. It seems natural, at first glance, to introduce a second fibre direction, $\boldsymbol{a}_2 \in \mathscr{B}_0$, in addition to the first fibre direction, $\boldsymbol{a}_1 \in \mathscr{B}_0$, with $\boldsymbol{a}_1 \times \boldsymbol{a}_2 \neq \boldsymbol{0}$, such that these vectors define two independent structural tensors of rank one, $\boldsymbol{A}_1 = \boldsymbol{a}_1 \otimes \boldsymbol{a}_1$ and $\boldsymbol{A}_2 = \boldsymbol{a}_2 \otimes \boldsymbol{a}_2$. Even though the purely elastic response for $\boldsymbol{A}_1$, $\boldsymbol{A}_2 = \text{const}$ and the set-up of appropriate evolution equations for $\lambda^{A_1} = \boldsymbol{a}_1 \cdot \boldsymbol{a}_1 = \boldsymbol{I} : \boldsymbol{A}_1$ and $\lambda^{A_2} = \boldsymbol{a}_2 \cdot \boldsymbol{a}_2 = \boldsymbol{I} : \boldsymbol{A}_2$, respectively, are self-evident as based on the framework developed in this contribution, the modelling of the reorientation of these two sets of fibres remains a non-trivial task. One promising approach for future research might consist in the incorporation of only one structural tensor of rank two; in other words

$$\begin{aligned} &\boldsymbol{A}_{12} = \boldsymbol{a}_1 \otimes \boldsymbol{a}_1 - \boldsymbol{a}_2 \otimes \boldsymbol{a}_2 \quad \text{and} \\ &||\boldsymbol{A}_{12}||^2 = [\lambda^{A_1}]^2 - 2[\boldsymbol{a}_1 \cdot \boldsymbol{a}_2]^2 + [\lambda^{A_2}]^2 > 0, \end{aligned} \tag{44}$$

where $\boldsymbol{a}_1 \cdot \boldsymbol{a}_2 \geq 0$ is assumed; see Zheng (1993) and Zheng and Spencer (1993) or Papadopoulos and Lu (2001), where special emphasis is placed on anisotropic elasto-plasticity. This ansatz is apparently less flexible than the introduction of two separate structural tensors $\boldsymbol{A}_1$ and $\boldsymbol{A}_2$, since the fibres are now either constrained to be

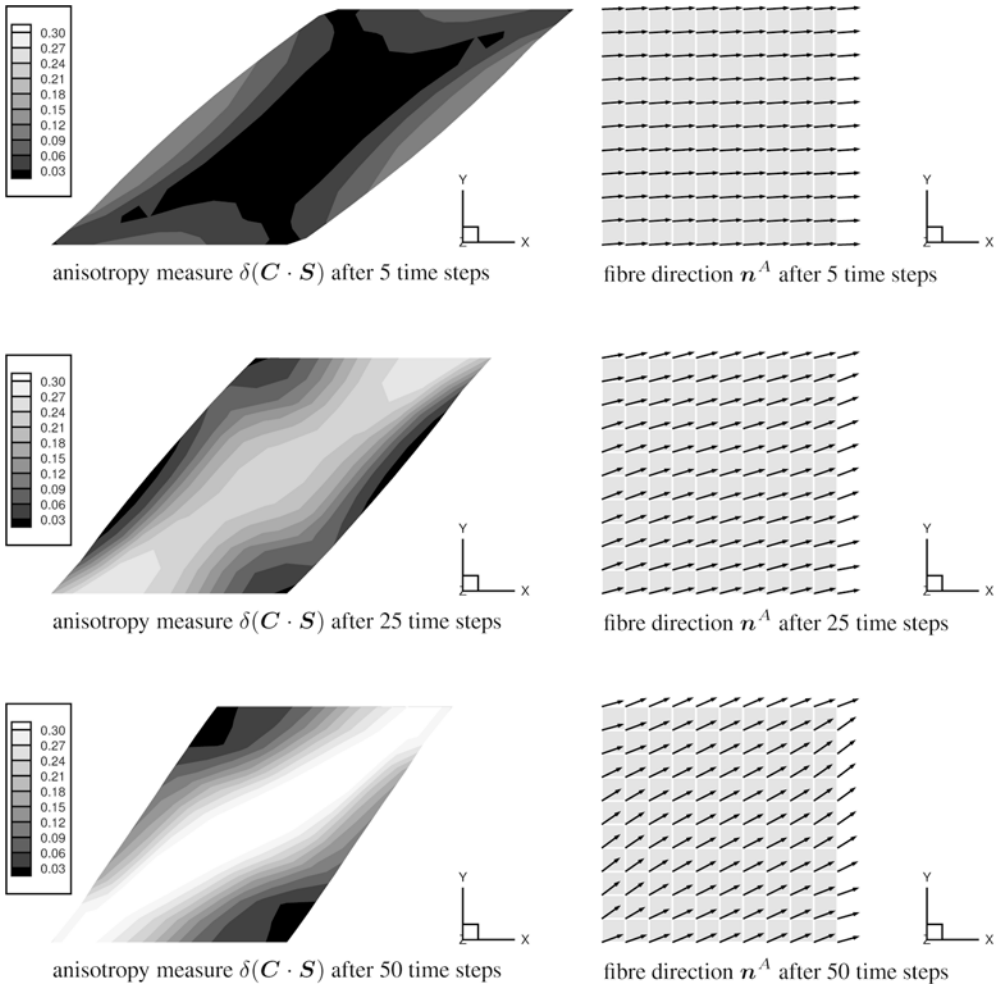

Fig. 14 Specimen under shear: anisotropy measure $\delta(\boldsymbol{C}\cdot\boldsymbol{S})$ (*left*) and fibre direction $\boldsymbol{n}^A$ (*right*) after 5, 25, and 50 time steps

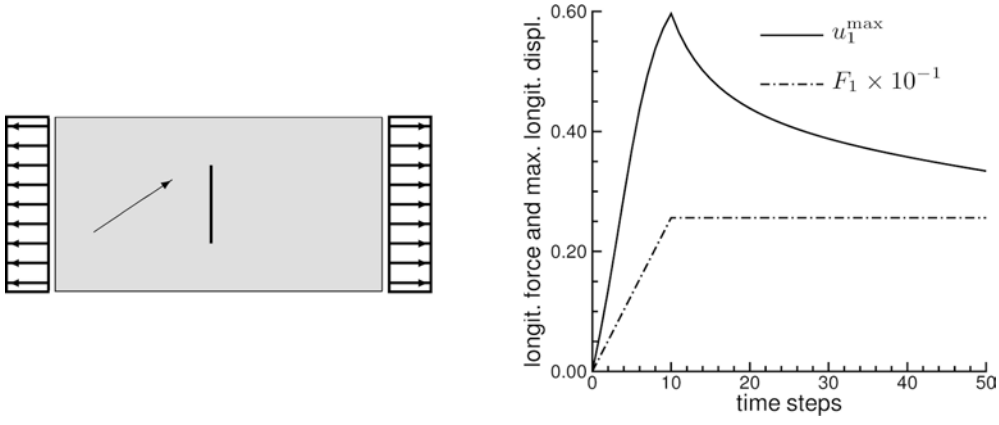

Fig. 15 Specimen with surface cut, $\phi_{\text{cut}} = 0$: geometry and boundary conditions (*left*), maximal longitudinal displacement $u_1{}^{\max}$ and loading history F_1 (*right*)

constantly perpendicular or to have identical properties. Besides the set-up of a reasonable evolution equation for λ^{A_1} and λ^{A_2} or $||\boldsymbol{A}_{12}||$, respectively, the remaining problem is the formulation of a physically motivated reorientation of the fibres. Practically speaking, we seek a particular representation of $||\boldsymbol{A}_{12}||^{-1}\boldsymbol{A}_{12} = \boldsymbol{R}(\Delta t\boldsymbol{\omega})\cdot[||\boldsymbol{A}_{k12}||^{-1}\boldsymbol{A}_{k12}]\cdot\boldsymbol{R}^t(\Delta t\boldsymbol{\omega})$, see also Sgarra and Vianello (1997), and recall Eq. 30. Following the ideas presented in this work, the (non-commutative) vector ω should therefore characterise the rotation, which maps the orthogonal frame $\{\boldsymbol{n}^{A_1}, \boldsymbol{n}^{A_2}, \boldsymbol{n}^{A_3}\}$ onto the principal directions of the appropriate strain field; with

$$\boldsymbol{n}^{A_1} = \left[\lambda^{A_1}\right]^{-\frac{1}{2}}\boldsymbol{a}_1, \quad \left[\lambda^{A_2}\right]^{-\frac{1}{2}}\boldsymbol{a}_2, \quad \boldsymbol{n}^{A_3} = \boldsymbol{n}^{A_1}\times\boldsymbol{n}^{A_2} \tag{45}$$

and $\boldsymbol{a}_1\cdot\boldsymbol{a}_2 = 0$ being obvious. If $\boldsymbol{a}_1\cdot\boldsymbol{a}_2 \neq 0$ and $\boldsymbol{a}_1\cdot\boldsymbol{a}_1 = \boldsymbol{a}_2\cdot\boldsymbol{a}_2 \doteq \lambda^A$, we can replace the corresponding non-orthogonal frame $\{\boldsymbol{n}^{A_1}, \boldsymbol{n}^{A_2}, \boldsymbol{n}^{A_3}\}$ by the orthogonal

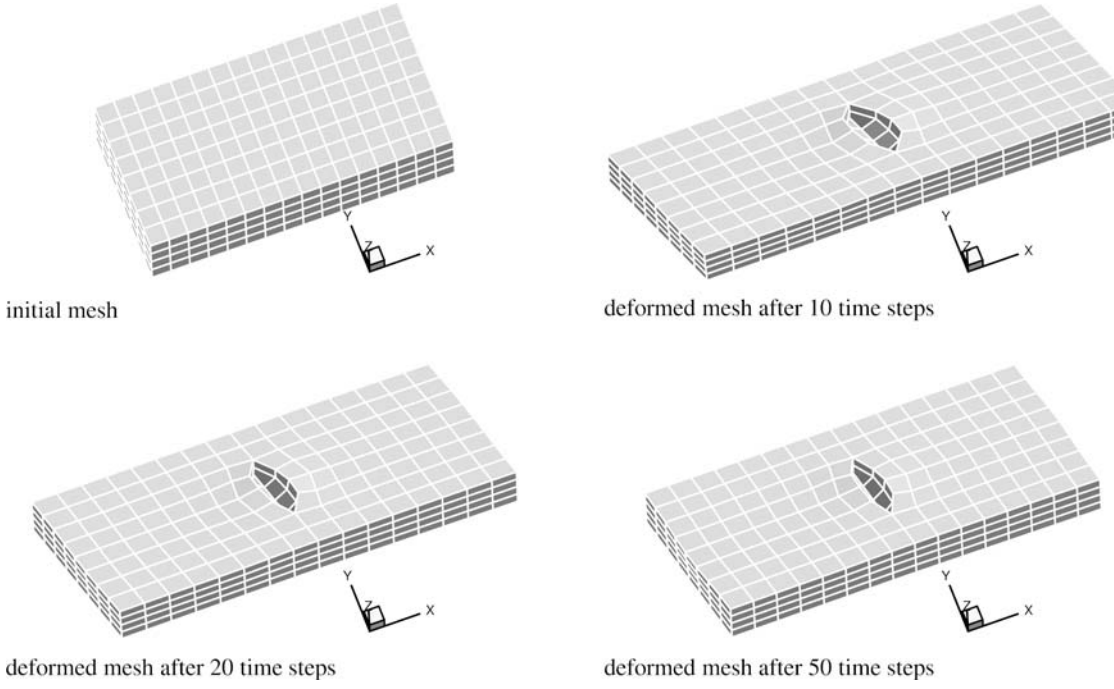

Fig. 16 Specimen with surface cut, $\phi_{\text{cut}} = 0$: initial mesh and deformed meshes after 10, 20, and 50 time steps

system $\left\{\bar{\boldsymbol{n}}^{A_1}, \bar{\boldsymbol{n}}^{A_2}, \bar{\boldsymbol{n}}^{A_3}\right\}$ defined via

$$2\bar{\boldsymbol{n}}^{A_1} = \left[\boldsymbol{n}^{A_1} + \boldsymbol{n}^{A_2}\right]/\cos(\gamma), \quad 2\bar{\boldsymbol{n}}^{A_2} = \left[\boldsymbol{n}^{A_2} - \boldsymbol{n}^{A_1}\right]/\sin(\gamma), \quad \bar{\boldsymbol{n}}^{A_3} = \bar{\boldsymbol{n}}^{A_1} \times \bar{\boldsymbol{n}}^{A_2} = \boldsymbol{n}^{A_3} \tag{46}$$

where $2\gamma = \boldsymbol{n}^{A_1} \cdot \boldsymbol{n}^{A2}$, see Spencer (1984) and also note the correlations $\boldsymbol{n}^{A_1} = \cos(\gamma)\bar{\boldsymbol{n}}^{A_1} - \sin(\gamma)\bar{\boldsymbol{n}}^{A_2}$ and $\boldsymbol{n}^{A_2} = \cos(\gamma)\bar{\boldsymbol{n}}^{A_1} + \sin(\gamma)\bar{\boldsymbol{n}}^{A_2}$, respectively. Based on this, we obtain (after some straightforward trig and algebra) the following alternative representation of the rank two structural tensor as an interesting side aspect

$$\begin{aligned}\bar{\boldsymbol{A}}_{12} &= [\bar{\boldsymbol{a}}_1 \otimes \bar{\boldsymbol{a}}_1 - \bar{\boldsymbol{a}}_2 \otimes \bar{\boldsymbol{a}}_2] \\ &= \lambda^A \left[\bar{\boldsymbol{n}}^{A_1} \otimes \bar{\boldsymbol{n}}^{A_1} - \bar{\boldsymbol{n}}^{A_2} \otimes \bar{\boldsymbol{n}}^{A_2}\right] \\ &= \lambda^A \left[\boldsymbol{n}^{A_1} \otimes \boldsymbol{n}^{A_2} + \boldsymbol{n}^{A_2} \otimes \boldsymbol{n}^{A_1} - \cos(2\gamma)\boldsymbol{n}^{A_1} \right. \\ &\quad \left. \otimes \boldsymbol{n}^{A_1} - \cos(2\gamma)\boldsymbol{n}^{A_2} \otimes \boldsymbol{n}^{A_2}\right] \times \left[1 - \cos^2(2\gamma)\right].\end{aligned} \tag{47}$$

7.3.3 Inverse problems

Finally, we almost do not need to mention that experiments will be of cardinal importance for extending the understanding of remodelling processes and to motivate at least some material parameters. Although such elaborate and complex experimental settings are rather difficult to implement, they appear to promise great benefits; for instance for tissue engineering applications as one practical example of the modelling of (hard and soft) biomaterials. A powerful framework is provided by the theory of (the corresponding) inverse problems, as addressed by Govindjee and Mihalic (1996, 1998) for example, where special emphasis is placed on hyperelasticity.

References

Almeida ES, Spilker RL (1998) Finite element formulations for hyperelastic transversely isotropic biphasic soft tissues. Comput Meth Appl Mech Eng 151:513–538

Ambrosi D, Mollica F (2002) On the mechanics of a growing tumor. Int J Eng Sci 40:1297–1316

Angeles J (1988) Rational kinematics. In: Springer tracts in natural philosopy, vol 34. Springer, Berlin Heidelberg New York

Antman SS (1995) Nonlinear problems of elasticity. In: Applied mathematical sciences, vol 107. Springer, Berlin Heidelberg New York

Ascher UM, Petzold LR (1998) Computer methods for ordinary differential equations and differential-algebraic equations. SIAM, Philadelphia, PA

Ball JM (1977) Convexity conditions and existence theorems in nonlinear elasticity. Arch Ration Mech Anal 63:337–403

Beatty MF (1987) A class of universial relations in isotropic elasticity theory. J Elast 17:113–121

Belytschko T, Liu WK, Moran B (2000) Nonlinear finite elements for continua and structures. Wiley, New York

Betsch P, Steinmann P (2002) Frame-indifferent beam finite elements based upon the geometrically exact beam theory. Int J Numer Meth Eng 54:1775–1788

Betsch P, Menzel A, Stein E (1998) On the parametrization of finite rotations in computational mechanics. A classification of concepts with application to smooth shells. Comput Meth Appl Mech Eng 155:273–305

Biot MA (1965) Mechanics of incremental deformations. Wiley, New York

Boehler JP (ed) (1987) Applications of tensor functions in solid mechanics. Number 292 in CISM courses and lectures. Springer, Berlin Heidelberg New York

Bowen RM (1976) Theory of mixtures. In: Eringen AC (ed) Continuum physics, vol III—Mixtures and EM field theories. Academic, New York, pp 1–127

Chadwick P (1999) Continuum mechanics. Dover, Mineola, NY

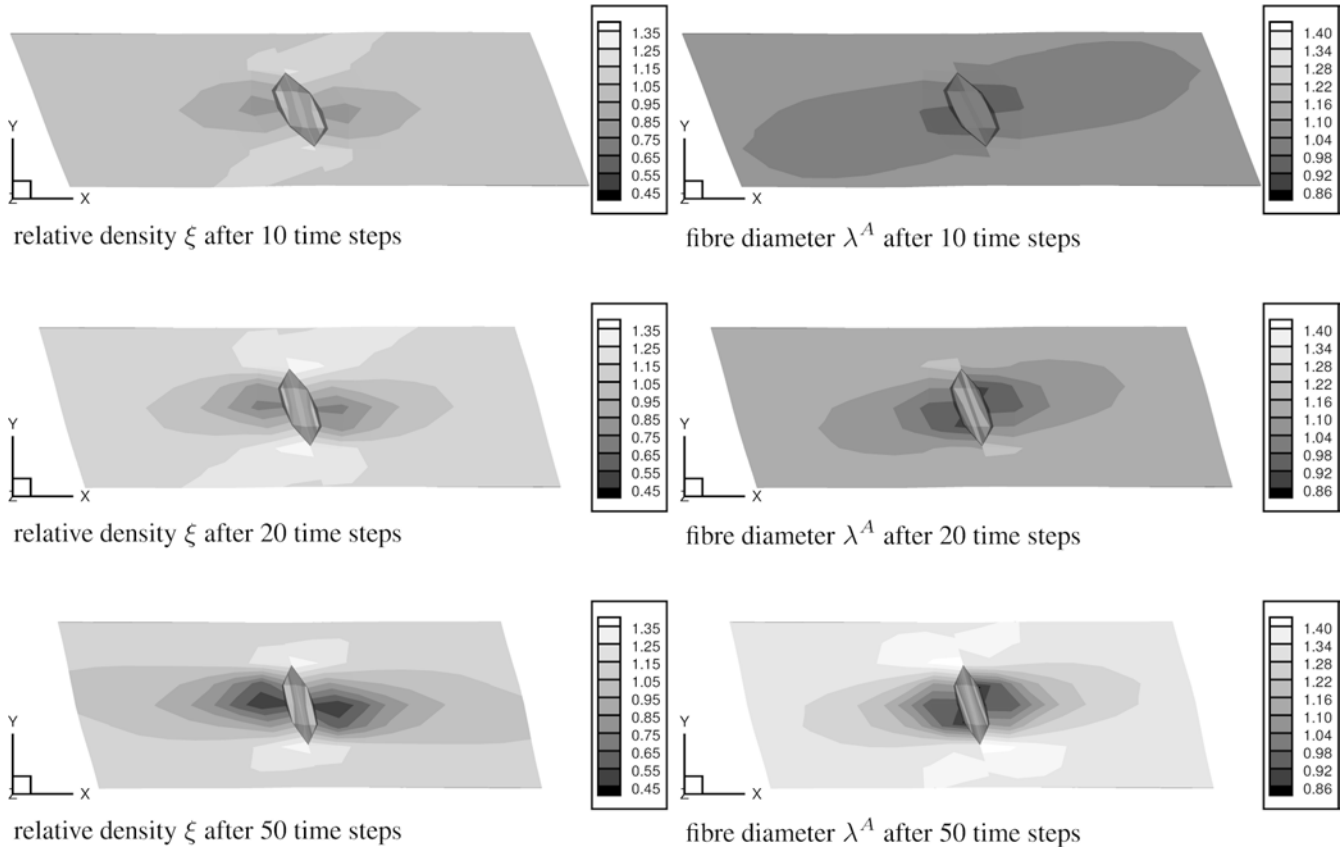

Fig. 17 Specimen with surface cut, $\phi_{\text{cut}} = 0$: relative density ξ (*left*) and fibre diameter λ^A (*right*) after 10, 20, and 50 time steps

Chen Y-C, Hoger A (2000) Constitutive functions of elastic materials in finite growth and deformation. J Elast 59:175–193

Ciarlet PG (1988) Mathematical elasticity—vol 1: three dimensional elasticity, vol 20 of studies in mathematics and its applications. North-Holland, Amsterdam

Ciarletta M, Iesan D (1993) Non-classical elastic solids In: Pitman research notes in mathematics series, vol 293. Longman, New York

Conti A, DeSimone A, Dolzmann G (2002) Soft elastic response of stretched sheets of nematic elastomers: a numerical study. J Mech Phys Solids 50:1431–1451

Cowin SC (1985) The relationship between the elasticity tensor and the fabric tensor. Mech Mater 4:137–147

Cowin SC (1994) Optimization of the strain energy density in linear anisotropic elasticity. J Elast 34:45–68

Cowin SC (1995) On the minimization and maximization of the strain energy density in cortical bone tissue. J Biomech 28(4):445–447, Technical note

Cowin SC (1996) Strain or deformation rate dependent finite growth in soft tissues. J Biomech 29(5):647–649, Technical note

Cowin SC (1997) Remarks on coaxiality of strain and stress in anisotropic elasticity. J Elast 47:83–84, Technical note

Cowin SC (1998) Imposing thermodynamic restrictions on the elastic constant-fabric tensor relationship. J Biomech 31:759–762, Technical note

Cowin SC (1999a) Bone poroelasticity. J Biomech 32:217–238

Cowin SC (1999b) Structural change in living tissues. Meccanica 34:379–398

Cowin SC (ed) (2001) Bone mechanics handbook, 2nd edn. CRC, Boca Raton, FL

Cowin SC, Hegedus DH (1976) Bone remodeling I: theory of adaptive elasticity. J Elast 6(3):313–326

Cowin SC, Humphrey JD (2000) Cardiovascular soft tissue mechanics. Kluwer, Dordrecht

Currey JD (2003) The many adaptions of bone. J Biomech 36:1487–1495

Dacorogna B (1989) Direct methods in the calculus of variations. In: Applied mathematical sciences, vol 78. Springer, Berlin Heidelberg New York

De Hart J, Peters GWM, Schreurs PJG, Baaijens FPT (2004) Collagen fibers reduce stresses and stabilize motion of aortic valve leaflets during systole. J Biomech 37:303–311

Dennis JE Jr, Schnabel RB (1996) Numerical methods for unconstrained optimization and nonlinear equations. In: Classics in applied mathematics, vol 16. SIAM, Philadelphia, PA

Dolzmann G (2003) Variational methods for crystalline microstructure—analysis and computation. Lecture notes in mathematics, vol 1803. Springer, Berlin Heidelberg New York

Driessen NJB, Peters GWM, Huyghe JM, Bouten CVC, Baaijens FPT (2003) Remodelling of continuously distributed collagen fibres in soft tissues. J Biomech 36:1151–1158. Erratum 36:1235

Epstein M, Maugin GA (2000) Thermomechanics of volumetric growth in uniform bodies. Int J Plasticity 16:951–978

Fellin W, Ostermann A (2002) Consistent tangent operators for constitutive rate equations. Int J Numer Anal Meth Geomech 26:1213–1233

Fung YC (1993) Biomechanics: mechanical properties of living tissues, 2nd edn. Springer, Berlin Heidelberg New York

Garikipati K, Narayanan H, Arruda EM, Grosh K, Calve S (2004) Material forces in the context of biotissue remodelling. In: Steinmann P, Maugin GA (eds) Mechanics of material forces. Euromech Colloquium 445 (preprint)

Gasser TC, Holzapfel GA (2003) A rate-independent elastoplastic constitutive model for biological fiber-reinforced composites at finite strains: continuum basis, algorithmic formulation and finite element implementation. Comput Mech 4–5:340–360

Giusti E (2003) Direct methods in the calculus of variantions. World Scientific, Singapore

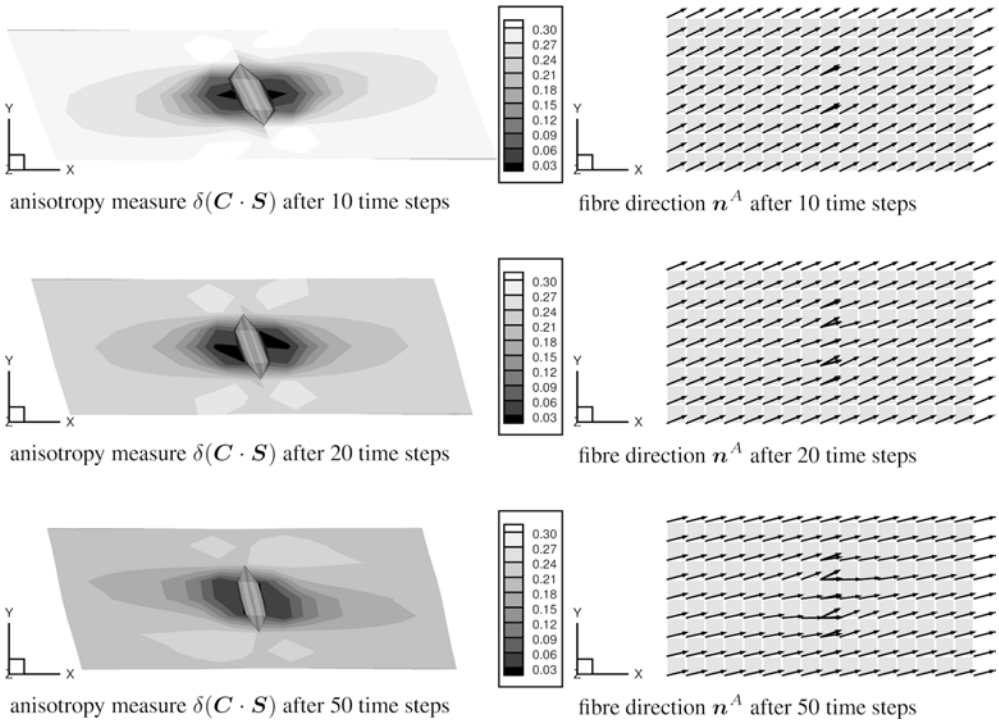

Fig. 18 Specimen with surface cut, $\phi_{\text{cut}} = 0$: anisotropy measure $\delta(\boldsymbol{C}\cdot\boldsymbol{S})$ (*left*) and fibre direction $\boldsymbol{n}^A$ (*right*) after 10, 20, and 50 time steps

Govindjee S, Mihalic A (1996) Computational methods for inverse finite elastostatics. Comput Meth Appl Mech Eng 136:47–57

Govindjee S, Mihalic A (1998) Computational methods for inverse deformations in quasi-incompressible finite elasticity. Int J Numer Meth Eng 43:821–838

Green AE, Rivlin RS, Shield RT (1952) General theory of small elastic deformations superposed on finite elastic deformations. Proc R Soc Lond Ser–A 211:128–154

de Groot SR (1961) Thermodynamics of irreversible processes. North Holland, Amsterdam

Harrigan TP, Hamilton JJ (1992) An analytical and numerical study of the stability of bone remodelling theories: dependence on microstructural stimulus. J Biomech 25(5):477–488 (corrigendum 26(3):365–366)

Harrigan TP, Hamilton JJ (1993) Finite element simulation of adaptive bone remodelling: a stability criterion and a time stepping method. Int J Numer Meth Eng 36:837–854

Harrigan TP, Hamilton JJ (1994) Necessary and sufficient conditions for global stability and uniqueness in finite element simulations of adaptive bone remodelling. Int J Solids Struct 31:97–107

Haupt P (2000) Continuum mechanics and theory of materials. Advanced texts in physics. Springer, Berlin Heidelberg New York

Haupt P, Pao Y-H, Hutter K (1992) Theory of incremental motion in a body with initial elasto-plastic deformation. J Elast 28:193–221

Hoger A (1993a) The constitutive equation for finite deformations of a transversely isotropic hyperelastic material with residual stress. J Elast 33:107–118

Hoger A (1993b) The dependence of the elasticity tensor on residual stress. J Elast 33:145–165

Hoger A (1993c) The elasticity tensors of a residually stressed material. J Elast 31:219–237

Hoger A (1996) The elasticity tensor of a transversely isotropic hyperelastic material with residual stress. J Elast 42:115–132

Hoger A (1997) Virtual configurations and constitutive equations for residually stressed bodies with material symmetry. J Elast 48:125–144

Holzapfel GA (2000) Nonlinear solid mechanics, a continuum approach for engineering. Wiley, New York

Holzapfel GA (2001) Biomechanics of soft tissue. In: Lemaitre J (ed) The handbook of materials behavior models. Multiphysics behaviors, vol 3, chapter 10, composite media, biomaterials, Academic, New York, pp 1049–1063

Holzapfel GA, Gasser TC (2001) A viscoelastic model for fibre-reinforced composites at finite strains: continuum basis, computational aspects and applications. Comput Meth Appl Mech Eng 190:4379–4403

Holzapfel GA, Ogden RW (eds) (2003) Biomechanics of soft tissue in cardiovascular systems. Number 441 in CISM courses and lectures. Springer, Berlin Heidelberg New York

Holzapfel GA, Gasser TC, Ogden RW (2000) A new constitutive framework for arterial wall mechanics and a comparative study of material models. J Elast 61:1–48

Huiskes R, Chao EYS (1983) A survey of finite element analysis in orthopedic biomechanics: The first decade. J Biomech 16(6):385–409

Humphrey JD (2002) Cardiovascular solid mechanics. Cells, tissues, and organs. Springer, Berlin Heidelberg New York

Husikes R, Weinans H, Grootenboer HJ, Dalastra M, Fudala B, Sloof TJ (1987) Adaptive bone-remodeling theory applied to prothetic-design analysis. J Biomech 20(11/12):1135–1150

Iesan D (1989) Prestressed bodies In: Pitman research notes in mathematics series, vol 195. Longman, New York

Imatani S, Maugin GA (2002) A constitutive model for material growth and its application to three-dimensional finite element analysis. Mech Res Commun 29:477–483

Jacobs CR, Levenston ME, Beaupré GS, Simo JC, Carter DR (1995) Numerical instabilities in bone remodelling simultaneous: the advantages of a node-based finite element approach. J Biomech 28(4):449–459

Jacobs CR, Simo JC, Beaupré GS, Carter DR (1997) Adaptive bone remodelling incorporationg simultaneous density and anisotropy considerations. J Biomech 30(6):603–613

Kaliske M (2000) A formulation of elasticity and viscoelasticity for fibre reinforced material at small and finite strains. Comput Meth Appl Mech Eng 185:225–243

Katchalsky A, Curran PF (1965) Nonequilibrium thermodynamics in biophysics. In: Harvard books in biophysics, vol 1. Harvard Univ Press, Cambridge, MA

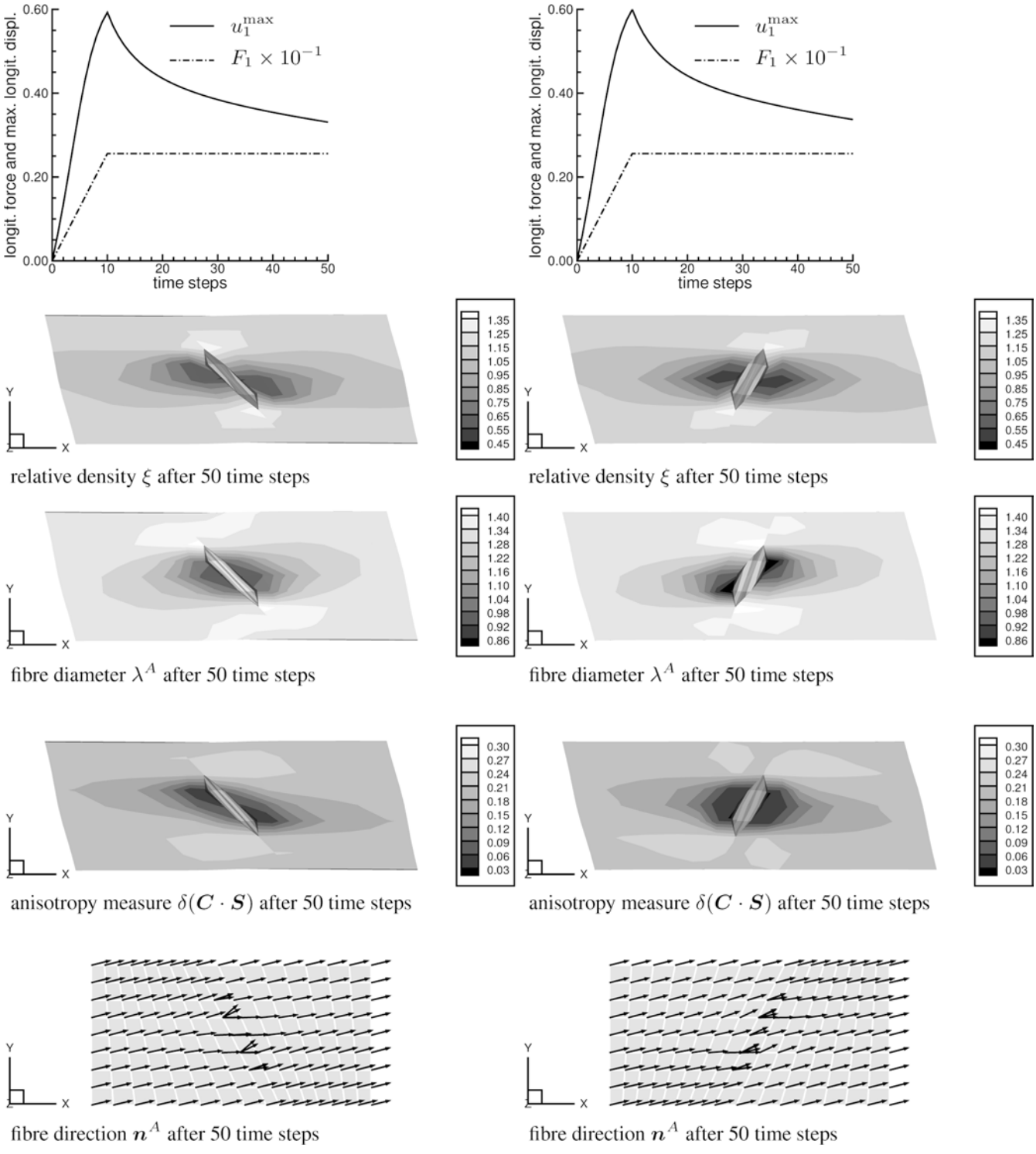

Fig. 19 Specimen with surface cut, $\phi_{\text{cut}} = \pi/6$ (*left*) and $\phi_{\text{cut}} = -\pi/6$ (*right*): load versus displacement curve ($F_1 \backslash u_1^{\max}$), anisotropy measure $\delta(\boldsymbol{C} \cdot \boldsymbol{S})$, fibre diameter λ^A and fibre direction $\boldsymbol{n}^A$ after 50 time steps

Kestin J (1966) A course in thermodynamics. Blaisdell, Waltham, MA

Krstin N, Nackenhorst U, Lammering R (2000) Zur konstitutiven Beschreibung des anisotropen beanspruchungsadaptiven Knochenumbaus. Techn Mech 20(1):31–40

Kuhl E, Steinmann P (2003a) Mass- and volume specific views on thermodynamics for open systems. Proc R Soc Lond Ser–A 459:2547–2568

Kuhl E, Steinmann P (2003b) On spatial and material settings of thermo-hyperelastodynamics for open systems. Acta Mech 160:179–217

Kuhl E, Steinmann P (2003c) Theory and numerics of geometrically nonlinear open system mechanics. Int J Numer Meth Eng 58:1593–1615

Kuhl E, Steinmann P (2004) Material forces in open system mechanics. Comput Meth Appl Mech Eng 193:2357–2381

Kuhl E, Menzel A, Steinmann P (2003) Computational modeling of growth—a critical review, a classification of concepts and two new consistent approaches. Comput Mech 32:71–88
Liu I-S (2002) Continuum mechanics. Advanced texts in physics. Springer, Berlin Heidelberg New York
Lubarda VA, Hoger A (2002) On the mechanics of solids with a growing mass. Int J Solids Struct 39:4627–4664
Maugin GA, Imatani S (2003a) Anisotropic growth of materials. J Phys IV France 105:365–372
Maugin GA, Imatani S (2003b) Material growth in solid–like materials. In: Miehe C (ed) Computational mechanics of solid materials at large strains, vol 108 of solid mechanics and its applications, IUTAM. Kluwer, Dordrecht, pp 221–234
Menzel A, Steinmann P (2001a) On the comparison of two strategies to formulate orthotropic hyperelasticity. J Elast 62:171–201
Menzel A, Steinmann P (2001b) A theoretical and computational setting for anisotropic continuum damage mechanics at large strains. Int J Solids Struct 38(52):9505–9523
Menzel A, Steinmann P (2003a) Geometrically nonlinear anisotropic inelasticity based on fictitious configurations: application to the coupling of continuum damage and multiplicative elasto-plasticity. Int J Numer Meth Eng 56:2233–2266
Menzel A, Steinmann P (2003b) On the spatial formulation of anisotropic multiplicative elasto-plasticity. Comput Meth Appl Mech Eng 192:3431–3470
Menzel A, Steinmann P (2003c) A view on anisotropic finite hyperelasticity. Euro J Mech A - Solids 22:71–87
Menzel A, Ekh M, Runesson K, Steinmann P (2004) A framework for multiplicative elastoplasticity with kinematic hardening coupled to anisotropic damage. Int J Plasticity (in press)
Merodio J, Ogden RW (2003) Instabilities and loss of ellipticity in fiber-reinforced compressible non-linearly elastic solids under plane deformation. Int J Solids Struct 40:4707–4727
Miehe C (1996) Numerical computation of algorithmic (consistent) tangent moduli in large-strain computational inelasticity. Comput Meth Appl Mech Eng 134:223–240
Murray JD (2002) Mathematical biology II: spatial models and biomedical applications. In: Interdisciplinary applied mathematics, vol 18, 3rd edn. Springer, Berlin Heidelberg New York
Nackenhorst U (1996) Numerical simulation of stress stimulated bone remodelling. Techn Mech 17(1):31–40
Oden JT (1972) Finite elements of nonlinear continua. In: Advanced engineering series. McGraw-Hill, New York
Ogden RW (1997) Non-linear elastic deformations. Dover, New York
Papadopoulos P, Lu J (2001) On the formulation and numerical solution of problems in anisotropic finite plasticity. Comput Meth Appl Mech Eng 190:4889–4910
Pérez-Foguet A, Rodriguez-Ferran A, Huerta A (2000a) Numerical differentiation for local and global tangent operators in computational plasticity. Comput Meth Appl Mech Eng 189:277–296
Pérez-Foguet A, Rodriguez-Ferran A, Huerta A (2000b) Numerical differentiation for non-trivial consistent tangent matrices: an application to the MRS–lade model. Int J Numer Meth Eng 48:159–184
Petersen P (1989) On optimal orientation of orthotropic materials. Struct Optim 1:101–106
Podio-Guidugli P (2000) A primer in elasticity. J Elast 58(1):1–103
Reese S, Raible T, Wriggers P (2001) Finite element modelling of orthotropic material behaviour in pneumatic membranes. Int J Solids Struct 38(52):9525–9544
Rodriguez EK, Hoger A, McCulloch D (1994) Stress-dependent finite growth in soft elastic tissues. J Biomech 27(4):455–467
Schneck DJ (1990) Engineering principles of physiological function. New York University Biomedical Engineering Series. New York University Press, New York
Schneck DJ (1992) Mechanics of muscle, 2nd edn. New York University Biomedical Engineering Series. New York University Press, New York
Schröder J, Neff P (2003) Invariant formulation of hyperelastic transverse isotropy based on polyconvex free energy functions. Int J Solids Struct 40:401–445
Sgarra C, Vianello M (1997) Rotations which make strain and stress coaxial. J Elast 47:217–224
Sherratt JA, Martin P, Murray JD, Lewis J (1992) Mathematical models of wound healing in embryonic and adult epidermis. IMA J Math Appl Med Biol 9:177–196
Šilhavý M (1997) The mechanics and thermomechanics of continuous media. Texts and monographs in physics. Springer, Berlin Heidelberg New York
Silver FH, Seehra GP, Freeman JW (2003) Collagen self-assemby and the development of tendon mechanical properties. J Biomech 36:1529–1553
Simo JC, Armero F (1992) Geometrically non-linear enhanced strain mixed methods and the method of incompatible modes. Int J Numer Meth Eng 33:1413–1449
Skalar R, Zargaryan S, Jain RK, Netti PA, Hoger A (1996) Compatibility and the genesis of residual stress by volumetic growth. J Math Biol 34:889–914
Skalar R, Farrow DA, Hoger A (1997) Kinematics of surface growth. J Math Biol 35:869–907
Spencer AJM (1984) Constitutive theory of strongly anisotropic solids. In: Spencer AJM (ed) Continuum theory of the mechanics of fibre-reinforced composites, CISM courses and lectures, vol 282. Springer, Berlin Heidelberg New York, pp 1–32
Taber LA (1995) Biomechanics of growth, remodelling, and morphogenesis. ASME Appl Mech Rev 48(8):487–545
Truesdell C (1966) Continuum mechanics I: the mechanical foundations of elasticity and fluid dynamics. In: International science review series, vol 8. Gordon and Beach, New York
Truesdell C, Noll W (2004) In: Antman SS (ed) The non-linear field theories of mechanics, 3rd edn. Springer, Berlin Heidelberg New York
Truesdell C, Toupin RA (1960) The classical field theories. In: Flügge S (ed) Encyclopedia of physics, vol III/1. Springer, Berlin Heidelberg New York, pp 226–793
Vianello M (1996a) Coaxiality of strain and stress in anisotropic linear elasticity. J Elast 42:283–289
Vianello M (1996b) Optimization of the stored energy and coaxiality of strain and stress in finite elasticity. J Elast 44:193–202
Weinans H, Huiskes R, Grootenboer HJ (1992) The behavior of adaptive bone-remodelling simulation models. J Biomech 25(12):1425–1441
Weiss JA, Maker BN, Govindjee S (1996) Finite element implementation of incompressible, transversely isotropic hyperelasticity. Comput Meth Appl Mech Eng 135:107–128
Weng S (1998) Ein anisotropes Knochenumbaumodell und dessen Anwendung. Techn Mech 18(3):173–180
Wren TAL (2003) A computational model for the adaption of muscle and tendon length to average muscle length and minimum tendon strain. J Biomech 36:1117–1124
Zheng Q-S (1993) On transversversely isotropic, orthotropic and relative isotropic functions of symmetric tensors, skew-symmetric tensors and vectors. Part I: two dimensional orthotropic and relative isotropic functions and three dimensional relative isotropic functions. Int J Eng Sci 31(10):1399–1409
Zheng Q-S, Spencer AJM (1993) Tensors which characterize anisotropies. Int J Eng Sci 31(5):679–693
Zysset PK (2003) A review of morphology—elasticity relationships in human trabecular bone: theories and experiments. J Biomech 36:1469–1485
Zysset PK, Curnier A (1995) An alternative model for anisotropic elasticity based on fabric tensors. Mech Mater 21:243–250